Clim Dyn (2008) 30:703–726
DOI 10.1007/s00382-007-0318-x

Leading patterns of the tropical Atlantic variability in a coupled general circulation model

Zeng-Zhen Hu · Bohua Huang · Kathy Pegion

Received: 1 May 2007 / Accepted: 12 September 2007 / Published online: 16 October 2007

Abstract This paper examines the mean annual cycle, interannual variability, and leading patterns of the tropical Atlantic Ocean simulated in a long-term integration of the climate forecast system (CFS), a state-of-the-art coupled general circulation model presently used for operational climate prediction at the National Centers for Environmental Prediction. By comparing the CFS simulation with corresponding observation-based analyses or reanalyses, it is shown that the CFS captures the seasonal mean climate, including the zonal gradients of sea surface temperature (SST) in the equatorial Atlantic Ocean, even though the CFS produces warm mean biases and underestimates the variability over the southeastern ocean. The seasonal transition from warm to cold phase along the equator is delayed 1 month in the CFS compared with the observations. This delay might be related to the failure of the model to simulate the cross-equatorial meridional wind associated with the African monsoon. The CFS also realistically simulates both the spatial structure and spectral distributions of the three major leading patterns of the SST anomalies in the tropical Atlantic Ocean: the south tropical Atlantic pattern (STA), the North tropical Atlantic pattern (NTA), and the southern subtropical Atlantic pattern (SSA). The CFS simulates the seasonal dependence of these patterns and partially reproduces their association with the El Niño-Southern Oscillation. The dynamical and thermodynamical processes associated with these patterns in the simulation and the observations are similar. The air-sea interaction processes associated with the STA pattern are well simulated in the CFS. The primary feature of the anomalous circulation in the Northern Hemisphere (NH) associated with the NTA pattern resembles that in the Southern Hemisphere (SH) linked with the SSA pattern, implying a similarity of the mechanisms in the evolution of these patterns and their connection with the tropical and extratropical anomalies in their respective hemispheres. The anomalies associated with both the SSA and NTA patterns are dominated by atmospheric fluctuations of equivalent-barotropic structure in the extratropics including zonally symmetric and asymmetric components. The zonally symmetric variability is associated with the annular modes, the Arctic Oscillation in the NH and the Antarctic Oscillation in the SH. The zonally asymmetric part of the anomalies in the Atlantic is teleconnected with the anomalies over the tropical Pacific. The misplaced teleconnection center over the southern subtropical ocean may be one of the reasons for the deformation of the SSA pattern in the CFS.

Z.-Z. Hu (✉) · B. Huang · K. Pegion
Center for Ocean-Land-Atmosphere Studies,
4041 Powder Mill Road, Suite 302, Calverton,
MD 20705, USA
e-mail: hu@cola.iges.org

B. Huang
Department of Climate Dynamics,
College of Science, George Mason University,
4400 University Drive, Fairfax, VA 22030, USA

1 Introduction

Compared to the El Niño-Southern Oscillation (ENSO) in the tropical Pacific Ocean, the interannual variability in the tropical Atlantic Ocean is moderate. Its mechanism may be more complicated because several ocean-atmospheric processes of comparable influence contribute to the observed leading anomalous sea surface temperature (SST) patterns. Tropical Atlantic variability (TAV) is affected

both by local air–sea interaction and remote forcing, such as ENSO, and is ultimately determined by the interaction of the local and remote effects (e.g., Zebiak 1993; Carton and Huang 1994; Ruiz-Barradas et al. 2000; Czaja et al. 2002; Illig et al. 2006; Chang et al. 2006). These processes are modulated by a dominant annual cycle. Due to this subtlety, it is still a challenge for current coupled general circulation models (CGCM) to capture the characteristics of TAV realistically (e.g., Breugem et al. 2006).

On the other hand, several recent studies have demonstrated the ability of some current CGCMs to simulate the major features of TAV to a certain degree. For instance, Huang et al. (2004) showed that their CGCM is able to reproduce the three observed leading SST anomaly (SSTA) patterns. A series of further studies (Huang et al. 2004; Huang and Shukla 2005; Hu and Huang 2006a) demonstrated that the model processes that generate these patterns are analogous to the observations. Using coupled systems of relatively low resolution, Wu et al. (2004) and Hazeleger and Haarsma (2005) also showed the capability of their models to reproduce these leading patterns. At this stage, however, the generality of these particular model results has yet to be demonstrated by a wider examination of other coupled systems, especially those used in major meteorological centers for operational climate prediction. This is necessary because the range of systematic errors is large for current CGCM simulated tropical climate in the Atlantic basin (Davey et al. 2002; Huang et al. 2007). For instance, some models are unable to reproduce the mean annual cycle of zonal SST gradient along the tropical Atlantic (Davey et al. 2002; Deser et al. 2006).

Recently, several meteorological research and operational centers have issued new generations of CGCMs (e.g., Wang et al. 2005; Deser et al. 2006; Delworth et al. 2006; Gnanadesikan et al. 2006; Jungclaus et al. 2006). In comparison to their predecessors, these new CGCMs typically have much higher horizontal and/or vertical resolutions for both the oceanic and atmospheric components and more updated sub-grid scale physical parameterizations. Generally, the simulation of the tropical Pacific climate and ENSO cycle is improved in these new versions. However, compared with their predecessors, it seems that the updated versions do not necessarily improve their simulation of the mean annual cycle or variability in the tropical Atlantic. For instance, Deser et al. (2006) noticed that the systematic biases of the zonal SST gradient in the tropical Atlantic Ocean in the recent version of the Community Climate System Model (CCSM) are similar to those from several previous versions. Thus, the quality of the simulation of TAV needs to be studied more deeply on a case-by-case basis.

In this study, we examine the mean annual cycle in the tropical Atlantic and its variability, as well as the leading patterns of TAV and their associated physical processes simulated by the climate forecast system (CFS) developed by the National Centers for Environmental Prediction (NCEP). It has been demonstrated that the CFS is reliable in simulating ENSO variability with realistic frequency (Wang et al. 2005). The amplitude of the simulated ENSO events is similar to that of observed strong events, even though the ENSO events in the simulation occur more regularly and persist longer than in the observations. Moreover, the CFS demonstrates considerable interseasonal predictability in hindcasts (Saha et al. 2006; Hu and Huang 2007b). We will show that in a long-term simulation, the CFS is able to realistically simulate the mean annual cycle and the leading patterns of SST variability in the tropical Atlantic as well as their seasonal dependence and associated physical processes. This study is complementary to our recent examination of the predictive skill of the CFS hindcasts in the Atlantic basin (Hu and Huang 2007b) and the evolution of the systematic biases in these hindcasts (Huang et al. 2007). We hope that our examination of this state-of-the-art coupled system will stimulate more interest in the simulation TAV in current CGCMs and more critical studies on the model capability in this aspect.

The paper is organized as follows. The model, data, and our analysis strategy are described in Sect. 2. Section 3 presents the results of the comparison of the simulation with the corresponding observations, including the mean annual cycle and interannual variability in the tropical Atlantic Ocean. Section 4 examines the major characteristics of the three leading patterns of TAV, their seasonal dependence and association with ENSO, and their connection with tropical and extratropical variations in the CFS and the observations. Section 5 summarizes our conclusions and briefly discusses the implications of this study.

2 Model, data, and analysis strategy

A coupled simulation of 52 years was conducted using the NCEP CFS at the Center for Ocean–Land–Atmosphere studies. The output of monthly data for the last 42 years after a 10-year spin-up are used in the following analyses. The atmospheric component of the CFS has horizontal resolution of T62 and 64 vertical sigma levels. The oceanic component is the GFDL Modular Ocean Model (Version 3, Pacanowski and Griffies 1998). The domain of the world oceans extends from 74°S to 64°N with a horizontal grid of $1° \times 1°$ poleward of 30°S and 30°N, and with gradually increased meridional resolution to 1/3° between 10°S and 10°N. Full interaction between the atmospheric and oceanic components is confined to 65°S to 50°N. Poleward of 74°S and 64°N, the atmosphere is forced by climatological SST. Between 74°S and 65°S and between 64°N and 50°N,

SST for the atmospheric component are the weighted average of the observed SST climatology and the SST from the ocean component. The ocean model has 40 levels vertically, with 27 of them in the upper 400 m. The atmospheric and oceanic components exchange daily averaged quantities, such as heat and momentum fluxes on a daily basis without flux adjustment. Details about the CFS and its systematic verification are given in Wang et al. (2005) and Saha et al. (2006).

For comparison with observations, we used the monthly mean data derived from the NCEP/NCAR reanalysis (Kalnay et al. 1996) and from the SST extended reconstruction (ERv2) on a 2° × 2° grid (Smith and Reynolds 2003). The data periods used in this investigation are from 1950 to 2003 for the reanalysis data, and from 1950 to 2005 for the ERv2 SST data. The analyzed net heat flux data at surface are from the comprehensive ocean–atmosphere data set (COADS) on a 1° × 1° grid in 1945–1993 (Woodruff et al. 1987; da Silva et al. 1994). The COADS is a collection of global marine surface observations taken primarily from ships and moored and drifting buoys. The precipitation data are the combination of satellite retrievals, in situ rain gauge stations, and atmospheric model products, analyzed by the Climate Prediction Center (Xie and Arkin 1996). This dataset spans from January 1979 to December 1998. In this work, these analyzed or reanalyzed data are referred to as observations. To focus on interannual time scales and also to suppress the long-term trend, a 10-year high-pass filter is applied to the analyzed and the CFS simulated data when analyzing the three leading patterns of TAV. The filter is based on a fast Fourier transform (Press et al. 1992).

In this study, we first compare the observations with the CFS simulated mean annual cycle and interannual variability [standard deviation (STDV)] of SST, wind stress, net heat flux at the surface, and total precipitation (Sect. 3). In Sect. 4, rotated empirical orthogonal function (REOF) analyses are conducted on all seasonal mean as well as specified seasonal mean SST in the tropical Atlantic (30°S–30°N) to derive the leading patterns of TAV. The REOFs are computed by the varimax method (Richman 1986) using the first 15 empirical orthogonal functions, which explain more than 80% of the total variance. The covariance matrixes are weighted by the square root of the grid box area prior to the REOF computation (North et al. 1982). We compute the regressions of surface wind stress and surface net heat flux onto the corresponding leading principal components (PCs) to examine the role of dynamical and thermodynamical processes associated with these leading patterns. We also compare the connection of these leading patterns with ENSO in the CFS and the observations and further study the temporal behavior and seasonality of these patterns for the simulated and observed SSTA. Furthermore, the connection of these leading patterns with anomalies in the tropical ocean and extratropical atmosphere is investigated.

3 Mean seasonal climate and variability

3.1 SST and wind stress at surface

Figures 1 and 2 show the CFS simulated and observed seasonal mean and the interannual variability (STDV) of SST and surface wind stress in the tropical Atlantic. The general pattern for the seasonal mean SST and surface wind stress is similar between the simulation and the observations. However, similar to some other CGCMs (Davey et al. 2002), the cold tongue is too weak and the Gulf of Guinea is too warm in the CFS simulation compared with the observations (Fig. 1). The westerly biases in the CFS simulated wind stress exist over the subtropical South Atlantic, particularly in JJA (Fig. 2). Furthermore, the interannual variability of SST and surface wind stress is not well simulated by the CFS, based on the STDV. The largest variability of SST occurs in the southeastern ocean in the observations, while in the CFS the interannual variability of SST is underestimated in this region (Fig. 1). For the variability of the wind stress, its larger values is mainly associated with trade winds in the subtropics and smaller ones mainly in the deep tropics (Fig. 2). The regions of underestimated variability of both SST and surface wind stress in the CFS are collocated with the large warm SST biases (see right column of Figs. 1, 2). The annual cycle of observed zonal gradient of SST as well as surface wind stress in the whole tropical Atlantic Ocean is qualitatively reproduced by the CFS (Figs. 1, 2). This is an improvement compared with previous CGCMs which simulated the wrong sign of the zonal gradient of annual mean SST (e.g., Davey et al. 2002; Deser et al. 2006).

The phase of the annual cycle of SST and surface wind stress along the equator is generally similar between the CFS and the observations (Fig. 3). The ocean cools down from boreal spring to boreal summer in both the CFS and the observations (Fig. 3a, b), consisting with Michell and Wallace (1992) (see their Figs. 6, 8, 12). However, the seasonal transition from warm SST to cold SST along the equator in the CFS lags 1 month behind the observations (Fig. 3a, b). The amplitude of the annual cycle of SST is slightly larger in the observations than in the CFS. The cold tongue does not extend to the coast in the CFS due to the fact that the eastern equatorial ocean is too warm in all seasons (Figs. 1, 3a, b). The annual cycle of surface wind stress in the CFS is also similar to the observations (Fig. 3c, d). Mitchell and Wallace (1992) argued that the increase in the northward surface winds in response to the

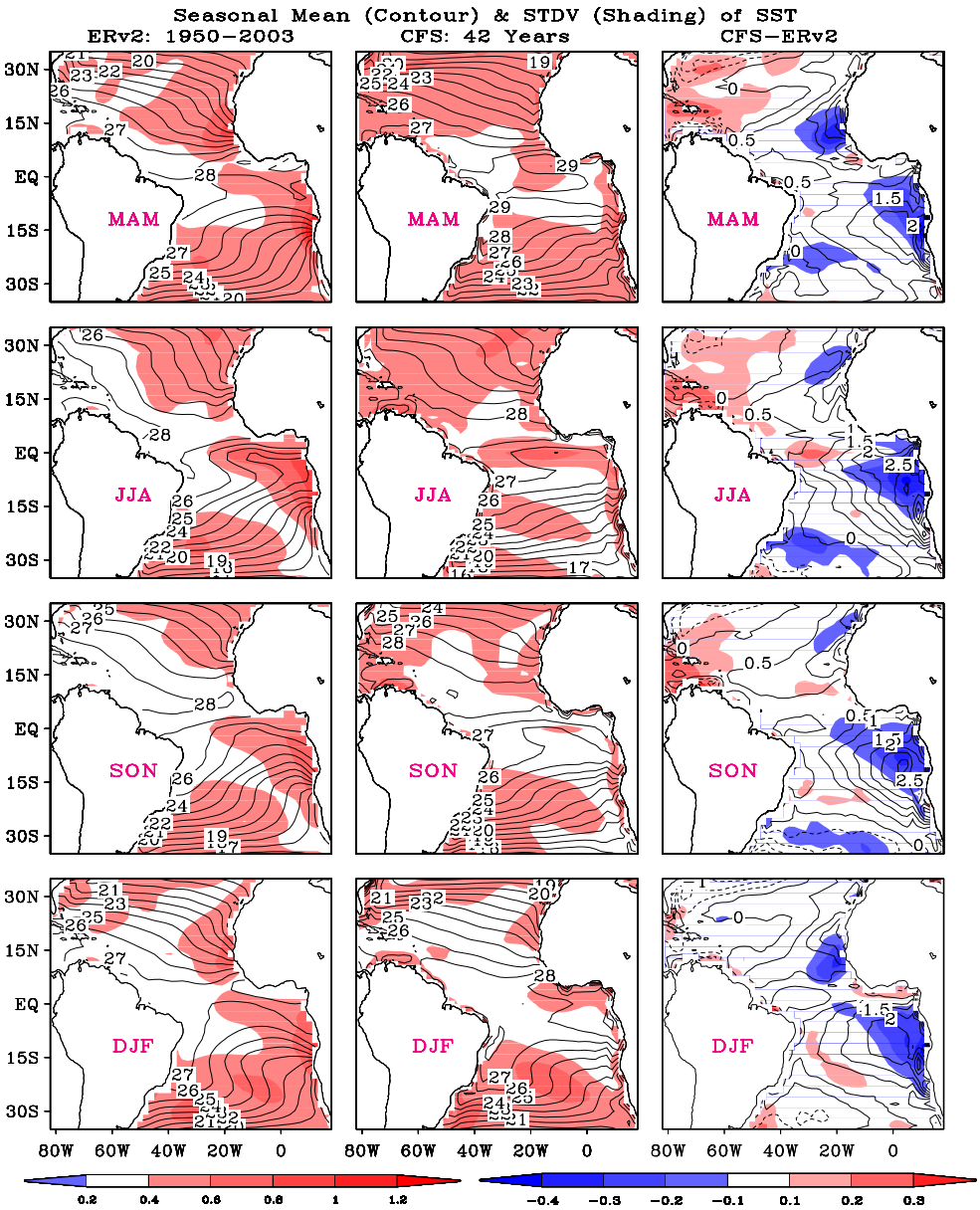

Fig. 1 Seasonal mean climatology (contour) and standard deviation (*STDV*) of SST (*shading*) of the ERv2 (*left column*) and the CFS simulation (*middle column*), and the difference of the CFS minus ERv2 (*right column*). The contour interval is 1°C for the mean SST and 0.5°C for the difference. The *left color bars* are for the means of the STDV and the *right color bars* for the differences of the STDV

onset of the northern summer monsoon may play a role in re-establishing the cold tongues in both the Pacific and Atlantic Oceans. Okumura and Xie (2004) also suggested that intensification of cross-equatorial southerlies associated with the onset of the African monsoon, in turn, triggers the oceanic cooling in the east. It is noted that the observed southerly surface wind stress in the southeastern Atlantic from March to June (Fig. 4c) is not reproduced in the CFS (Fig. 4d). The absence of the southerly winds in May–June (Fig. 4d) may be associated with the persistent warm bias in the southeastern ocean from the last fall to spring. The excessive warm SST in the south reduces the land–sea temperature contrast between the west African continent and the eastern tropical Atlantic Ocean. In boreal spring, this seems to lead to a delayed outbreak of the west Africa monsoon and hence the southerlies over the eastern Atlantic. Stronger than observed southerly winds near the equator are seen in the model during July–October (Fig. 4d), which should cool the sea surface down by enhancing the surface evaporation. At this period, however, the warm biases in the southeastern ocean are mainly driven by excessive short-wave solar heat flux reaching the sea surface due to an underestimation of low clouds in this area (Huang et al. 2007, Hu et al. 2007c). It is this SST bias that persists into the next year and delays the monsoon outbreak.

Both the phase and amplitude of the annual cycle of SST and surface wind stress along 15°S are well reproduced in the CFS (Fig. 4). Choosing 15°S is due to the fact that the largest biases of SST in the tropical Atlantic are at about 15°S

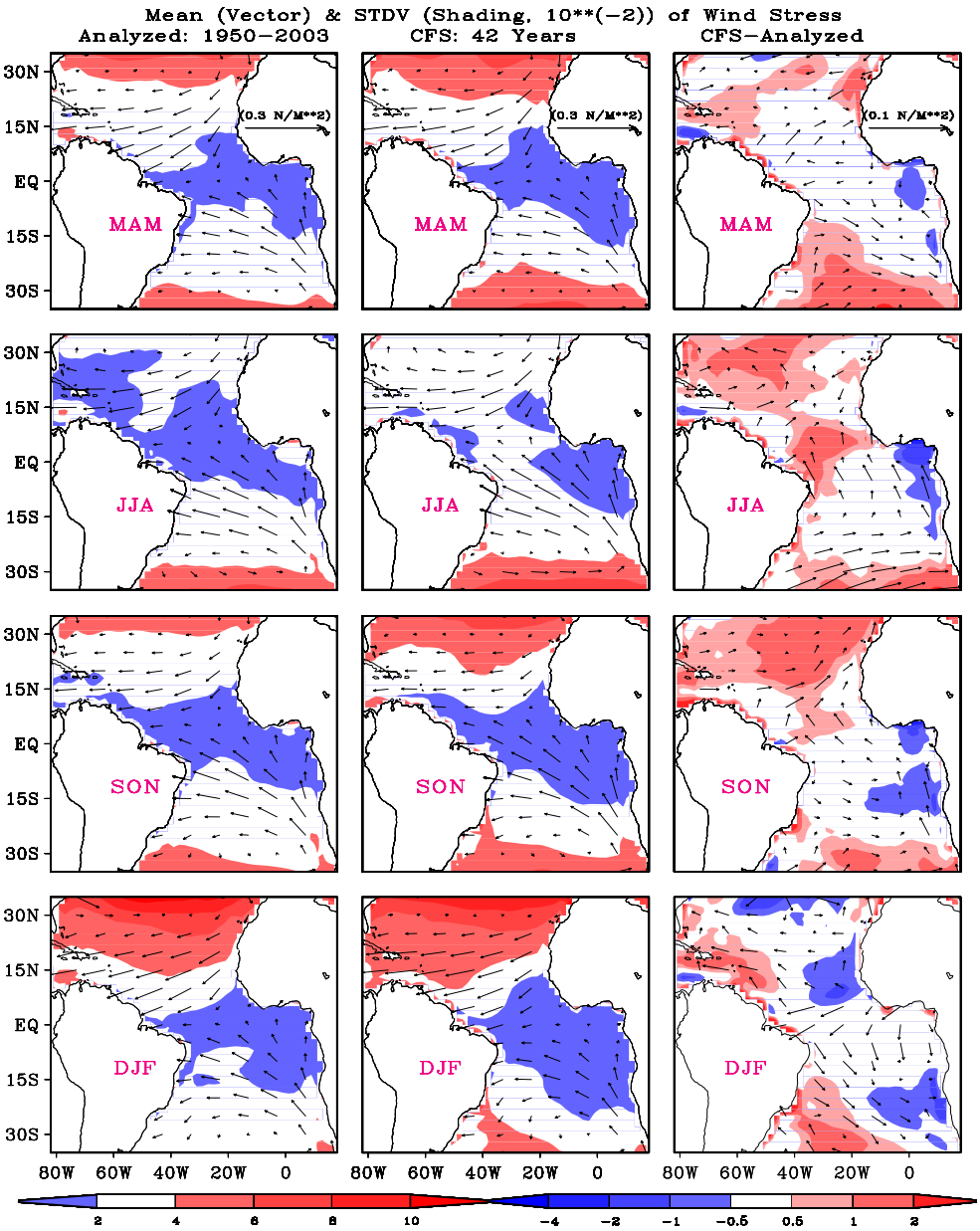

Fig. 2 Seasonal mean climatology (*vector*) and STDV of wind stress (*shading*) of the NCEP/NCAR reanalyses (*left column*) and the CFS simulation (*middle column*), and the difference of the CFS minus the reanalyses (*right column*). The values are enlarged 100 times for the STDV with unit of newton per square meter. The *left color bars* are for the means of the STDV and the *right color bars* for the differences of the STDV

(Fig. 1). The warmest (coldest) seasons occur along the eastern boundary of the ocean from February to April (July to September) in both the observations (Fig. 4a) and the CFS (Fig. 4b). The largest warming (cooling) seasons coincide with the period of northerly (southerly) surface wind stress (Fig. 4). This is consistent with the results of previous investigations, such as, Mitchell and Wallace (1992) for observational study and Okumura and Xie (2004) for model simulations. However, the cold SST anomalies during June to November display a strong westward propagation in the observations (Fig. 4a), which is not seen in the CFS (Fig. 4 b). Furthermore, there are warm biases in the eastern ocean in the CFS both along the equator and in the subtropics (Fig. 1). These are likely caused or amplified by the underestimation of low clouds in the CFS in this region (Huang et al. 2007). The underestimation of low clouds in the CFS is associated with incorrect vertical temperature stratification in the lower troposphere, which has been investigated in Hu et al. 2007c. These warming biases are seasonally dependent and reach their peak in November and December in the southeastern Atlantic Ocean reported by Huang et al. (2007) based on the CFS hindcasts. These warm biases may lower the predictive skill of the CFS in that region (Hu and Huang 2007b).

3.2 Heat flux at surface and total precipitation

Similarly, the CFS reproduces the observed general spatial patterns of the mean annual cycle of net downward total heat flux at the surface (Fig. 5) and total precipitation

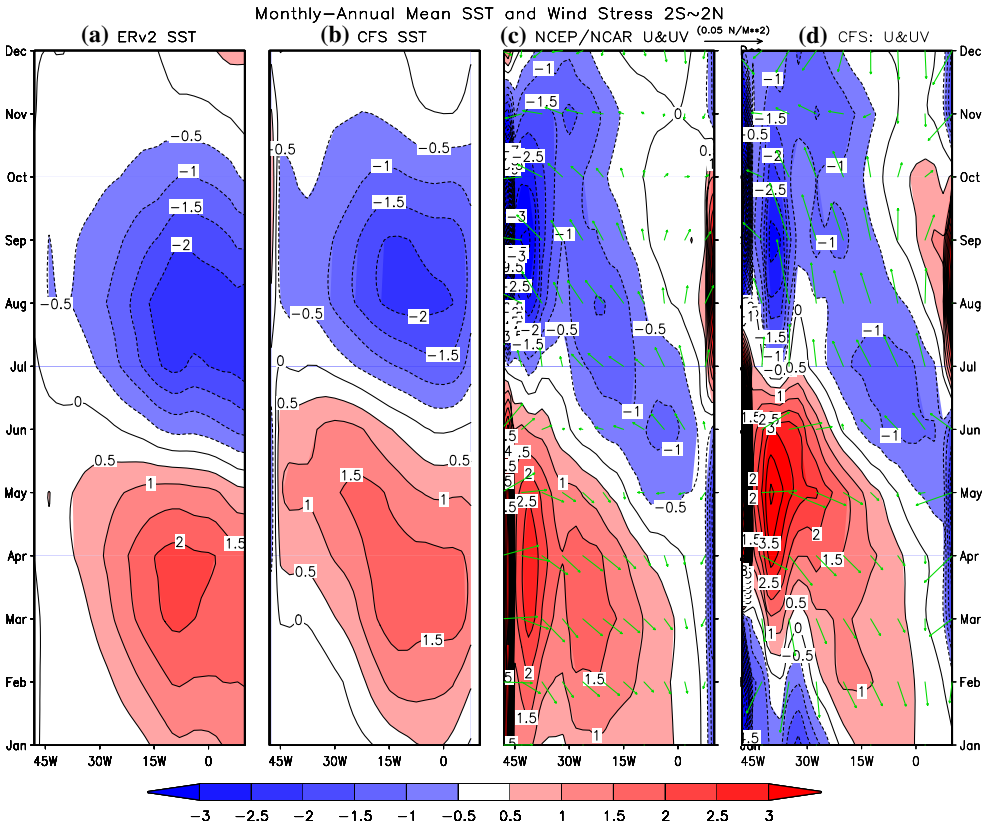

Fig. 3 Monthly mean minus annual mean SST (*left two columns*), surface wind stress (*vector*) and its u-component (*shading and contour*) (*right two columns*) averaged in 2°S–2°N of ERv2 analyzed (**a**), NCEP/NCAR reanalyzed (**c**), the CFS simulated (**b**, **d**). The values of the u-component are enlarged 100 times in plotting. The contour interval is 0.5°C for the SST, and 0.005 N/m^2 for the u-component

(Fig. 6). For the heat flux, the positive (negative) values are located in the hemisphere with stronger (weaker) sunshine, due to a dominant role of surface solar radiation in the heat flux (Fig. 5). On average, the differences of the net downward total heat flux between the CFS and the COADS are in a range of 20–60 W/m^2 (see right column of Fig. 5). The difference reaches –80 W/m^2 in the southern side of the equatorial ocean in JJA, which is consistent with the large precipitation bias there (Fig. 6). That may suggest that the bias in the net total heat flux at the surface in the CFS may be mainly due to the bias in the radiation component, caused by the incorrected simulation of the precipitation and clouds. The variability of the heat flux is generally smaller near the equator than in the subtropics, likely due to latent heat flux associated with mid-latitude weather noise. The variability of the the heat flux is clearly underestimated in the CFS, particularly in the tropical South Atlantic (see right column of Fig. 5), partially consisting with that of SST and wind stress (right column of Figs. 1, 2). Due to the fact that the net heat flux at the surface shown in Fig. 5 is interactively determined with the active involvement of the oceanic state variables, such as SST itself, the magnitude of the net heat flux alone can not explain the SST biases shown in Fig. 1. In order to explain the role of the surface heat flux on the SST biases, the contribution of individual component to the local heat balance should be examined. The influences of the local heat fluxes toward the CFS SST bias in this region have been examined by a previous study using the CFS climate hindcasts (Huang et al., 2007). Through an examination of the contributions of the heat flux components toward the SST tendency that leads the model SST from the realistic initial conditions to the biased state, Huang et al. (2007) have concluded that the excessive solar radiation is the major driving force. The contribution of individual components of the surface heat flux into the leading variability modes in the tropical Atlantic Ocean have been examined in author's previous works (Hu and Huang, 2006a, 2006b, 2007a).

For the total precipitation, except for DJF (December, January, and February), the CFS reproduces the position of maximum precipitation, implying a correct simulation of the location of the intertropical convergence zone (ITCZ) (Fig. 6). On the average, the CFS simulates a too strong ITCZ. In DJF, the simulated ITCZ is shifted southward and the two large precipitation centers in the western North and South Atlantic do not exist in the corresponding observations. Moreover, the double-ITCZs are still seen in MAM (March, April, and May) and JJA. The variability of the precipitation is largely overestimated, particularly over the southwestern North Atlantic and northwestern South Atlantic. This may be due to the fact that the precipitation

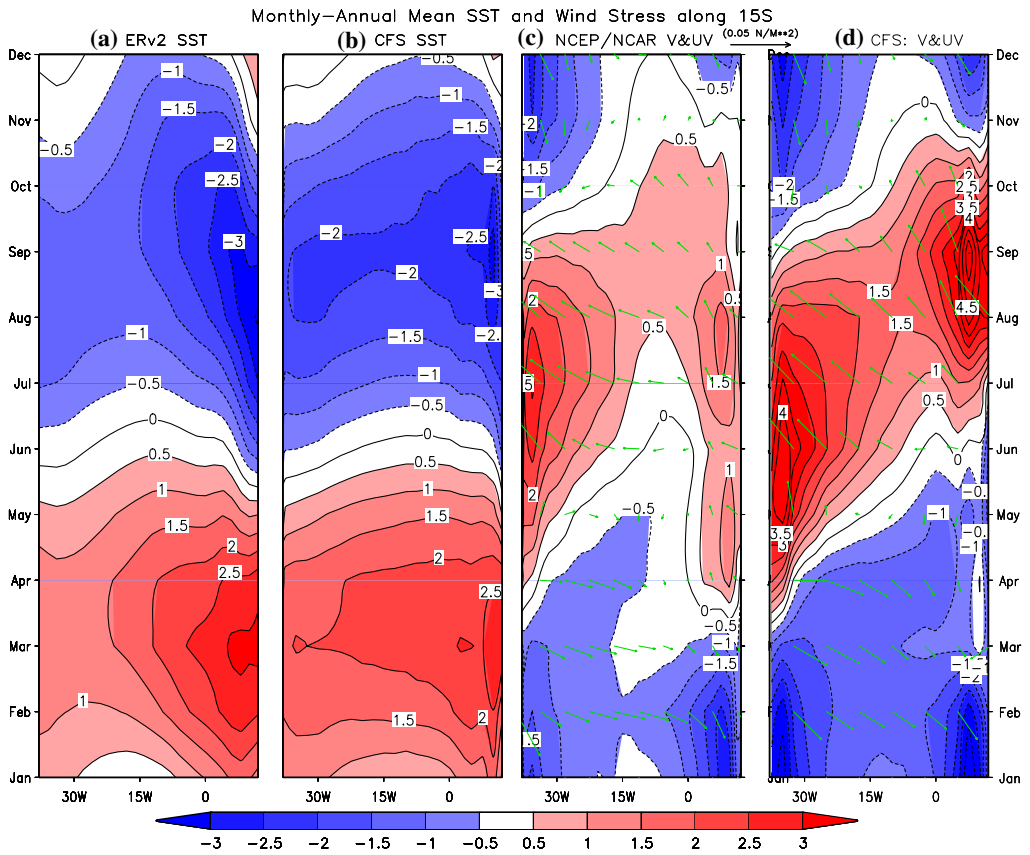

Fig. 4 Monthly mean minus annual mean SST (*left two columns*), surface wind stress (*vector*) and its v-component (*shading and contour*) (*right two columns*) along 15°S of ERv2 analyzed (**a**), NCEP/NCAR reanalyzed (**c**), the CFS simulated (**b**, **d**). The values of the v-component are enlarged 100 times in plotting. The contour interval is 0.5°C for the SST, and 0.005 N/m^2 for the v-component

is more sensitive to the warm bias in the warm tropical western ocean than in the cold tropical eastern ocean. The variability along the equator in the CFS simulations is too large in JJA and too small in DJF (Fig. 6). The precipitation biases may be mainly associated with the mass-flux cumulus parameterization scheme used in the CFS (Hong and Pan 1998, Saha et al, 2006). The CFS uses a version of the relaxed Arakawa–Schubert scheme for its parameterization of the deep convection. Based on our previous examination of the CFS hindcast, the model provides a better-than-average simulation of the ITCZ position and precipitation amount (Huang et al., 2007). A major problem is a southward shift of the ITCZ in boreal spring to about 10°S, which, however, may be a response to the local warm bias generated by other processes. A potential influence of the deep convection on the SST bias in the south is the strength of the subsidence branch of the convectively driven Hadley cell that caps the local shallow convection. However, a full investigation of this issue is beyond the scope of this work.

Overall the CFS reproduces the mean annual cycle of SST, wind stress, net heat flux at the surface, and total precipitation. The main spatial patterns of the variability of some of these variables are partially simulated. Systematic errors are seen in both the mean state and the variability. The major biases of the CFS are in the southeastern ocean with too warm mean SST and too small variability of SST, wind stress and net heat flux at the surface. The seasonal transition from warm to cold phase along the equator is delayed 1 month in the CFS compared with the observations. The major biases in precipitation are associated with the intensity and location of the ITCZ. The ITCZ is overestimated in the CFS, particularly in the tropical western ocean.

4 Leading patterns of variability

4.1 Basic features of the leading patterns of variability

The variability in the tropical Atlantic is composed of three main patterns which will be compared between the CFS and the observations. Figure 7 shows the first three leading REOFs of the ERv2 analyzed and the CFS simulated seasonal mean SSTA. Superimposed are contemporaneous regressions of surface wind stress anomalies onto the

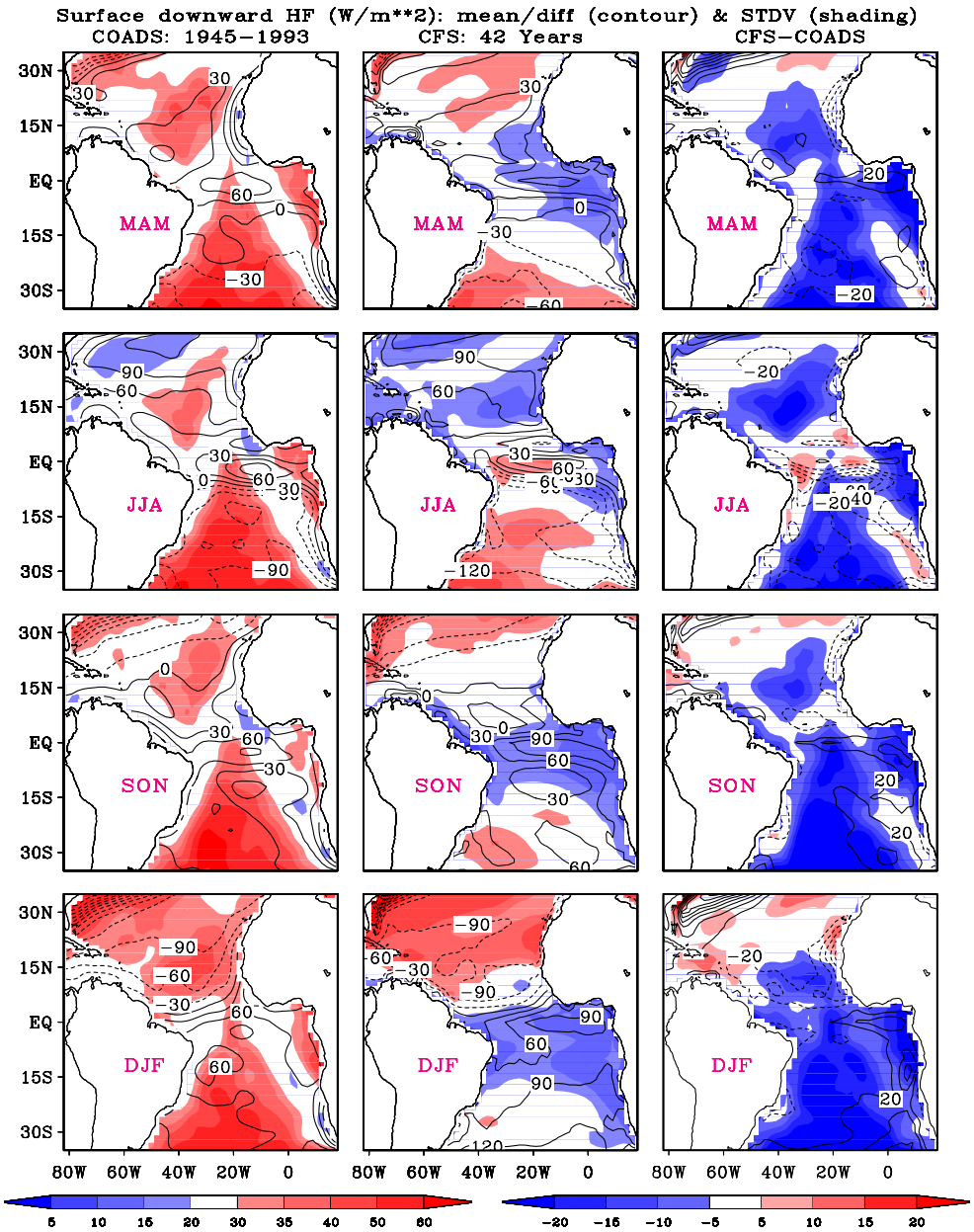

Fig. 5 Seasonal mean climatology of downward heat flux at the surface (*contour*) and its STDV (*shading*) of the COADS data (*left column*) and the CFS simulation (*middle column*), and the difference of the CFS minus the COADS (*right column*). The contour interval is 30 W/m^2 for the mean and 20 W/m^2 for the difference. The *left color bars* are for the means of the STDV and the *right color bars* for the differences of the STDV

corresponding PCs. Although the sequence and the percentages of the explained variance are different between the leading REOFs of the ERv2 analyzed and the CFS simulated SSTA, the major patterns of interannual variability of tropical Atlantic SSTA are well reproduced. Following the terminology used in Huang et al. (2004), the spatial pattern in the top panels of Fig. 7 is hereafter referred to as the southern tropical Atlantic (STA) pattern, in the middle panels the northern tropical Atlantic (NTA) pattern, and in the bottom panels the southern subtropical Atlantic (SSA) pattern. One should note that these are not generally accepted names for the dominant patterns of TAV, and these patterns have different names in the literature. For instance, the NTA pattern is also called gradient mode or hemispheric mode and the STA pattern is often called as Atlantic El-Nino or equatorial cold tongue mode. The SSA pattern is generally considered as the tropical lobe of the South Atlantic dipole, which is referred to as the opposite SST anomalies between 0–30°S and 30–40°S and is associated with the fluctuation of the strength of the subtropical anticyclone (See Fig. 10 in Venegas et al. 1997). The following analyses show that the dynamical and thermodynamical processes associated with each pattern are similar in the CFS simulation and the observations.

The frequency spectrum of each of the leading patterns of SST variability is simulated reasonably well by the CFS (Fig. 8). It should be noted that, to focus on interannual variability and to eliminate the influence of climate drift in

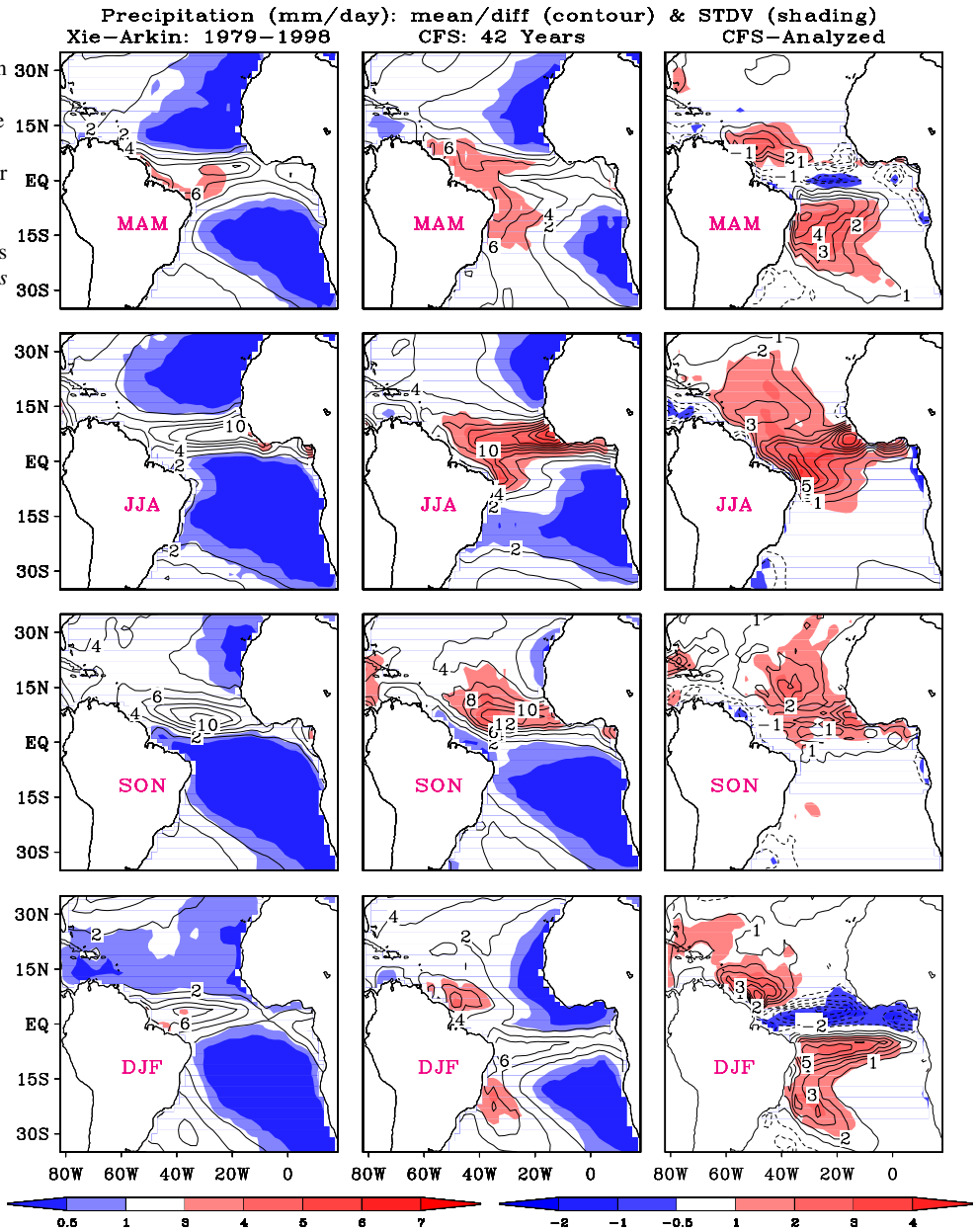

Fig. 6 Seasonal mean climatology of total precipitation (*contour*) and its STDV (*shading*) of the Xie-Arkin analyses (*left column*), the CFS simulation (*middle column*), and the difference of the CFS minus the analyses (*right column*). The contour interval is 2 mm/day for the mean and 1 mm/day for the difference. The *left color bars* are for the means of the STDV and the *right color bars* for the differences of the STDV

the model, a 10-year high-pass filter is applied to the simulated and observed SST data prior to the REOF calculations. At the 90% significance level, the major significant periods of the STA pattern are mainly in the band of 1–2 years in the observed SST, and in a slightly broader band in the simulation. For the NTA pattern, the dominant periods are 2.5 years in the observed SST and 3–4 years in the simulated SST. The significant periods of the SSA pattern are centered at 5 years in both the observed and simulated SSTA. These results are generally consistent with the results of both model and observation studies, such as, Huang et al. (2004) and Wu et al. (2004).

By computing the variances of the first three leading PCs for each season (Fig. 9), it is seen that the CFS largely reproduces the seasonal dependence of the strengths of the leading patterns. In both the observed and simulated SST, the STA pattern is the strongest in JJA (June, July, and August), the NTA pattern is the most active in MAM, and the SSA pattern is the strongest in DJF (Fig. 9). The strongest SSA pattern occurred in DJF is consistent with the fact that the air–sea coupling in the South Atlantic is most significant during the Southern Hemisphere (SH) summer (Venegas et al. 1997). By examing the leading coupled modes in the South Atlantic in observations, Venegas et al. (1997) argued that the coupling is strongest

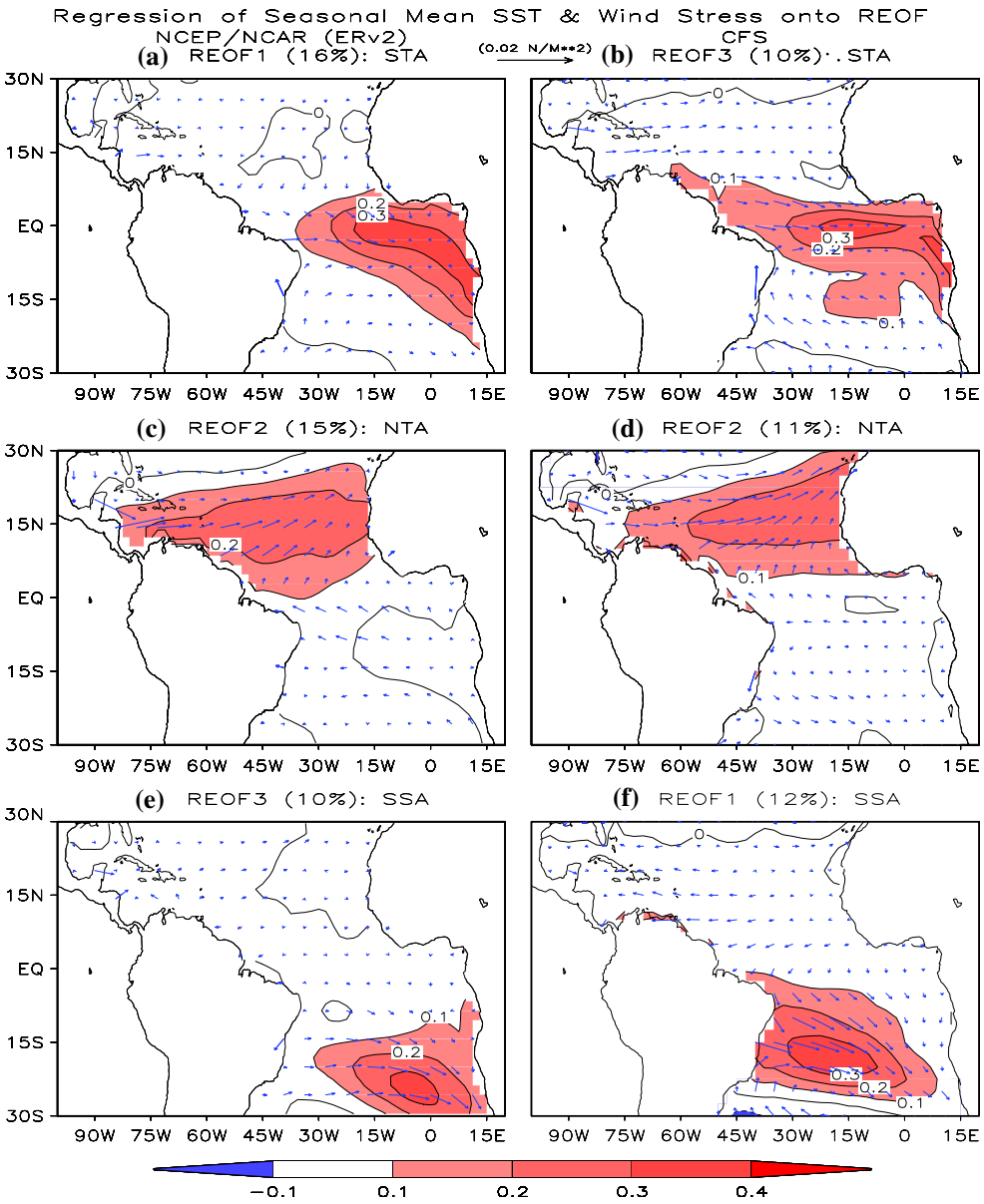

Fig. 7 Spatial patterns (*shading and contour*) of REOFs of ERv2 (*left columns*) and the CFS simulated (*right columns*) seasonal mean SST in the tropical Atlantic (30°S–30°N, 100°W–20°E). The vectors represent the simultaneous regression of seasonal mean wind stress onto the corresponding time series of the REOF. The contour interval is 0.1°C. The percentage of the variance explained by each pattern is indicated at the *top of each panel*

during the SH summer because of possible links with major climatic oscillations observed in the Northern Hemisphere (NH), such as, the North Atlantic Oscillation (NAO), Pacific-North American pattern (PNA), which are strongest during the NH winter. On the other hand, the seasonal cycle of the local oceanic mixed layer favors a stronger SH summer response to the atmospheric heat flux forcing even if the latter holds steady throughout a year. Seasonally, the oceanic mixed layer in this region is relatively shallow in SH summer and to a certain extent decoupled from the fossil layer below the seasonal thermocline. Therefore, the surface heat flux is most effective in driving the SST in SH summer because it warms up a relatively shallow layer with minimum entrainment from below. In addition, the CFS also correctly simulates the least active season of the NTA pattern in SON (September, October, November). However, the CFS does not reproduce the seasons with the weakest activity of the STA and SSA patterns.

These leading patterns in the tropical Atlantic are also affected by the ENSO (e.g., Enfield and Mayer 1997; Huang et al. 2002; Chang et al. 2006). The CFS is partially able to reproduce the relationship. For instance, the impact of ENSO on the NTA pattern is well captured by the CFS in both the magnitude of the correlation and their lead-lag relation (Fig. 10b). The maximum influence occurs when ENSO leads the NTA pattern by 4–6 months in both the observations and simulation. This impact is the most significant among the three patterns. However, the connection of ENSO with the STA and SSA patterns (Fig. 10a, c) is not well simulated. The relationship is not in phase

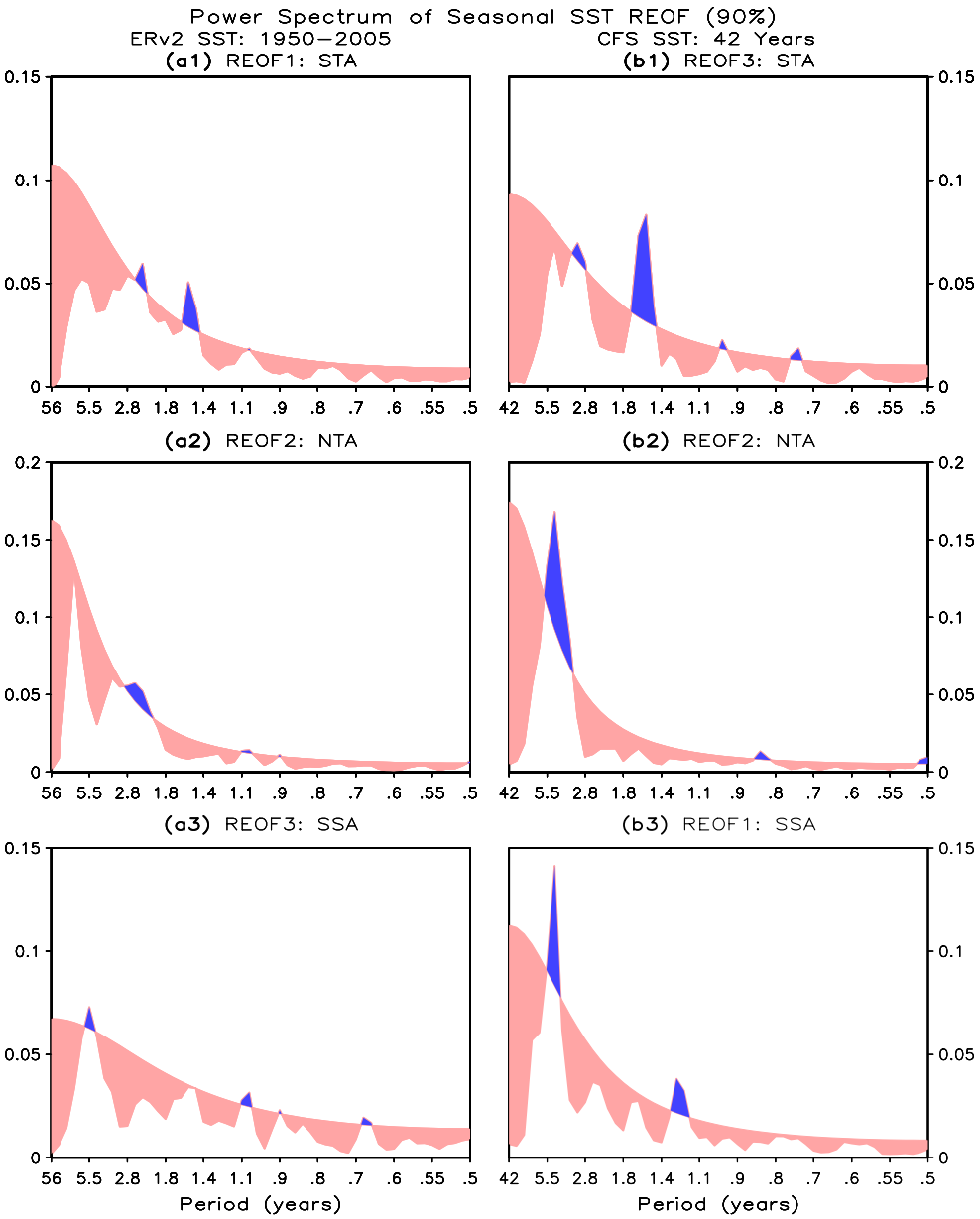

Fig. 8 Power spectrum and significance test (at 90%) of the time series of first three REOFs for the STA (*top panels*), NTA (*middle panels*), and SSA (*bottom panels*) patterns in the ERv2 analyzed (*left column*) and the CFS simulated (*right column*) SSTA

between the observations and the CFS. For the SSA pattern, the ENSO influence reaches its peak when the lead is zero for the observations, but the peak occurs when ENSO leads the SSA pattern by about 12 months in the CFS (Fig. 10c). The connection is also too strong in the CFS compared with the observations. These problems may be related to the deficiencies of the ENSO simulation in the CFS (Wang et al. 2005). For instance, the amplitude of ENSO is too large, and on average, simulated warm events tend to start about 3 months earlier and persist longer than observed. Therefore, it seems impossible to correctly simulate the ENSO-TAV relationship by a model which does not correctly simulate ENSO. Furthermore, the difference of the ENSO and SSA relationship between the CFS and the observations (Fig. 10c) is particularly large, which might be due to the fact that the ENSO influence in the tropical South Atlantic is overestimated in the CFS (Hu and Huang 2007b).

4.2 Equatorial thermodynamics and dynamics

The variability of the STA pattern is associated with anomalous westerly wind stress anomalies along the equator to the west of the SSTA center (top panels of Fig. 7), which are similar between the regressions of simulation and observations. These winds play an important role in the development of the STA pattern (Hu and Huang

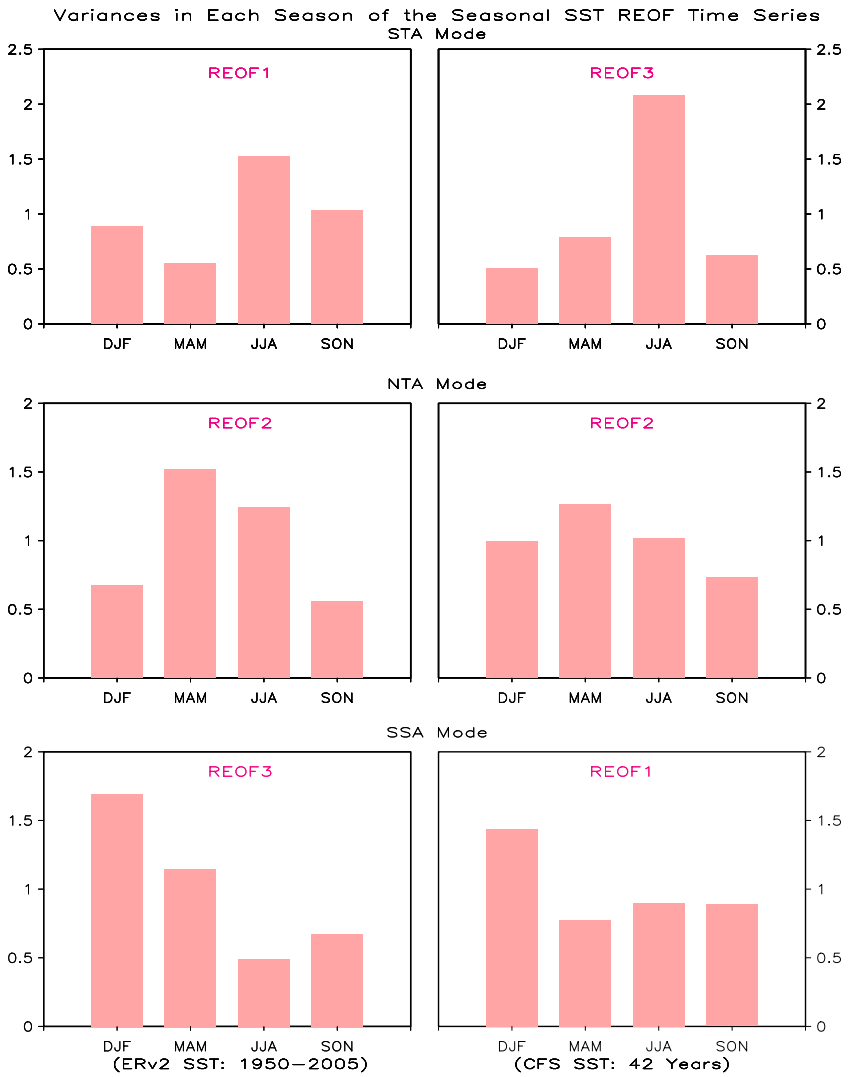

Fig. 9 Variances of the time series of first three REOFs for each season for the STA (*top panels*), NTA (*middle panels*), and SSA (*bottom panels*) patterns in the ERv2 analyzed (*left column*) and the CFS simulated (*right column*) SSTA

2007a). The surface winds converge toward the SSTA center. The associated net surface heat flux into the ocean is also similar between the regressions of simulation and observations: negative heat flux appears in the SH and the negative center exists along the equatorial central ocean (top panels of Fig. 11). The maximum heat loss in the regression of net surface heat flux is larger than 8 W/m^2 per STDV of the corresponding time series. Strong ocean heat loss (top panels of Fig. 11) is generally collocated with strong warm anomalies (top panels of Fig. 7), indicating a negative feedback of thermodynamical processes on the evolution of the STA pattern. Some differences are noted in the observations and simulation. For example, the ocean gains some heat from the atmosphere in the western equatorial ocean in the observations (Fig. 11a), while in the simulation this is seen in the tropical NH near the equator (Fig. 11b). In addition, the orientation of the maximum cooling of heat flux is analogous to that in SSTA. It is southeast-northwest in the observations (Figs. 7a, 11a) and zonal in the simulation (Figs. 7b, 11b). This is also agreed with the westward propagation of seasonal mean SST in the southeastern ocean (Fig. 4a). Overall, the SSTA is primarily driven by dynamical processes and the thermodynamical processes mainly act to damp the SSTA in the development of the STA pattern. This scenario is consistent with Huang et al. (2004) and Hu and Huang (2007a). The connection of this pattern with SST, ocean heat content, and wind stress at the surface will be further examined later in this subsection.

The development of the NTA pattern is linked with strong southwesterly anomalies in the tropical North Atlantic in both the observations and simulation (middle panels of Fig. 7). The southwesterly anomalies weaken the northeasterly trade-winds in the climatology (Fig. 2). This favors a positive feedback of the wind speed-evaporation-SST (WES) mechanism (Xie and Philander 1994; Chang et al. 1997; Xie 1999), which develops through the mutual enhancement among the anomalies of the SST gradient,

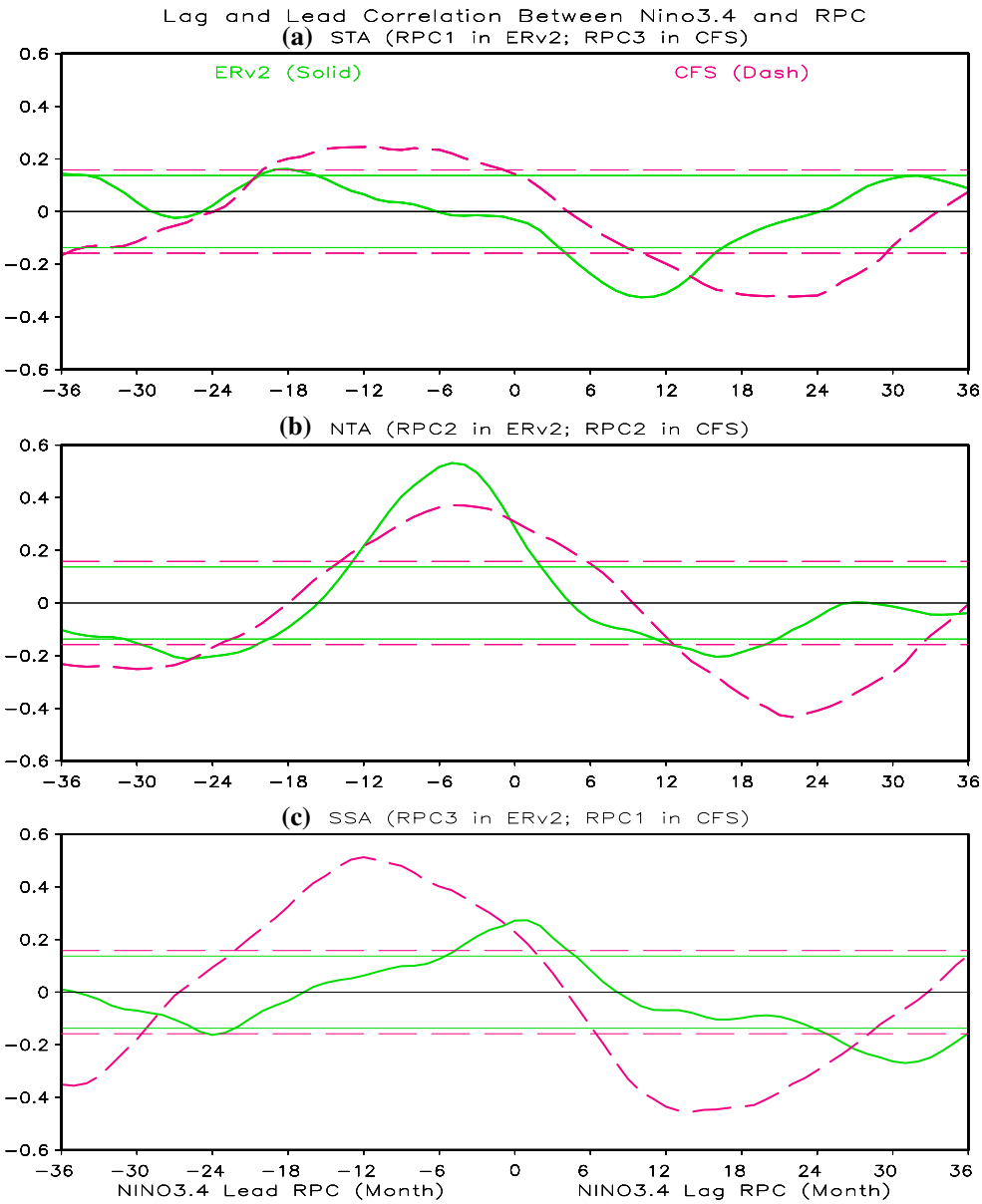

Fig. 10 Lag and lead correlations between Nino3.4 index and the REOF time series corresponding to the STA (**a**), NTA (**b**), and SSA (**c**) patterns in Fig. 7. *Solid (dash) lines* are the correlations of Nino3.4 with the time series using ERv2 (CFS) SSTA and the corresponding significance test at 95% level. The negative (positive) values along the abscissa represent months of the Nino3.4 index leading (lagging) the time series

wind stress, and latent heat flux. The regressions of net surface heat flux of 2 months prior to the corresponding NTA pattern show large positive values in the tropical North Atlantic (middle panels of Fig. 11), which are collocated with the large SSTA (middle panels of Fig. 7). The maximum of the regression of net surface heat flux is larger than 4–6 W/m^2 per STDV of the corresponding time series. This indicates a strong thermodynamical forcing on the development of the NTA pattern. This agrees with the result of Huang and Shukla (2005) and Hu and Huang (2006a, 2006b). They demonstrated the role of thermodynamical processes in the evolution of the NTA patterns in both model simulation and observations. In both the model simulation and the observation, the tropical North Atlantic (5–20°N) gains heat from the atmosphere. A major difference between the regressions using the observations and the simulation occurs in the equatorial and tropical South Atlantic. The tropical South Atlantic Ocean (0–25°S) loses heat to the atmosphere in the observations, while the equatorial Atlantic Ocean gains heat from the atmosphere and the associated heat flux is small in the tropical South Atlantic in the simulation (middle panels of Fig. 11). This difference is likely due to the differences in the associated wind stress shown in Figs. 7c and d, which will be discussed further in the next paragraph.

The NTA and SSA patterns are mainly driven by variations in the trade winds which for the NTA is related to the NAO (e.g., Czaja et al 2002) and for the SSA pattern to

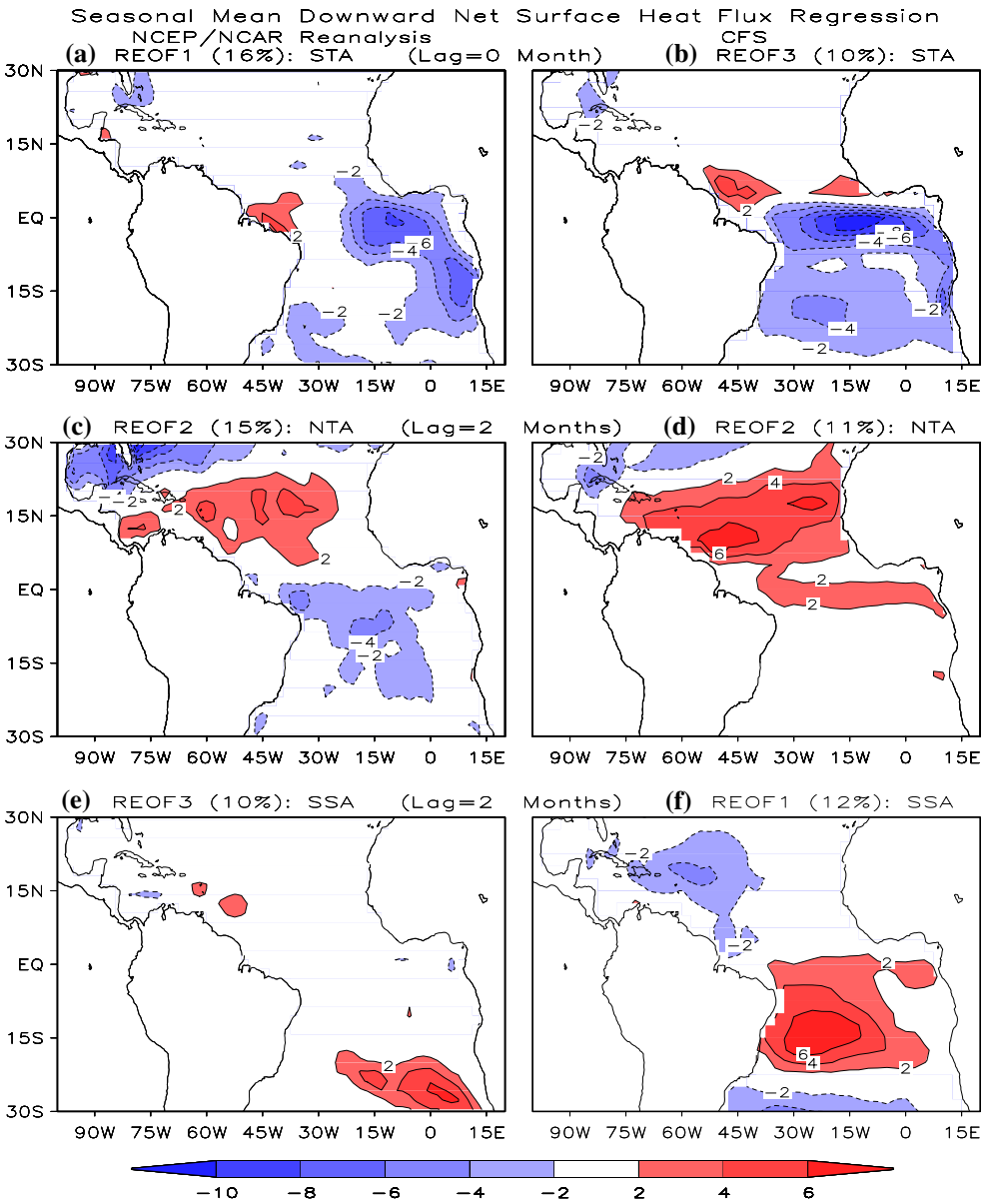

Fig. 11 The regression of seasonal mean net downward heat flux at surface onto the time series corresponding to the REOFs in Fig. 7. The regressions associated with the STA pattern are simultaneous and with the NTA and SSA patterns the heat flux leads by 2 months. The contour interval is 2 W/m^2 per STDV of the corresponding REOF time series. The zero line is suppressed

the south Atlantic subtropical high (e.g., Sterl and Hazeleger 2003), which will be further examined in the next subsection. The WES feedback is important in amplifying the response (Xie and Philander 1994; Chang et al. 1997; Xie 1999; Hu and Huang 2006a; 2006b). It is noticed that the WES feedback for the NTA pattern is much weaker in the CFS than in the observations. There is clearly cross-equatorial flow in the wind stress in the observations (Fig. 7c), whereas it is absent in the CFS (Fig. 7d). The associated anomalous southeasterlies in the observations in the southern ocean enhances the trade wind and favors cooling down the ocean. This explains the difference of the heat flux in the South Atlantic between the observations and the CFS (Fig. 11d). The maximum of the regression of net surface heat flux associated with the NTA and SSA patterns reaches 4–6 W/m^2 per STDV of the corresponding time series in both the CFS and the observations. It is noted that the SSA pattern in the simulation (Fig. 7f) is shifted northwestward compared with the corresponding one in the observations (Fig. 7e). The analyses in subsection 4.3 will show that the misplaced teleconnection center over the southern subtropical ocean may be one of the reasons for the deformation of the SSA pattern in the CFS.

The physical processes associated with the STA pattern are further investigated by examining the lagging and leading correlation of ATL3 index with SST and wind stress (Fig. 12a) and heat content (Fig. 12b) along the equator in the CFS. The ATL3 index is defined as the SSTA averaged in 3°S–3°N, 0°–20°W (Zebiak 1993). The ATL3 index represents the feature of air–sea interaction in

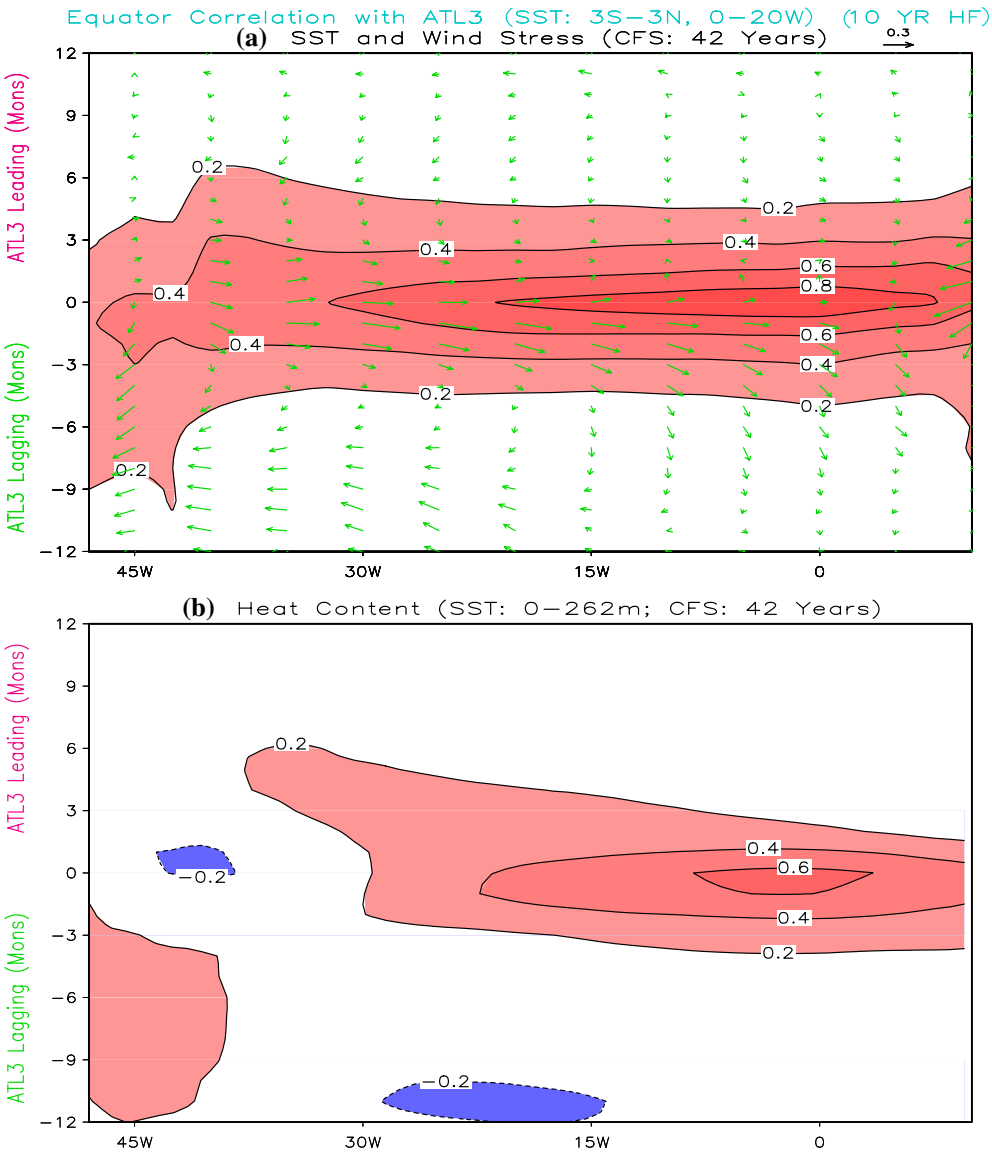

Fig. 12 Lagging and Leading correlation of ATL3 index (SSTA averaged in 3°S–3°N, 0–20°W) with SST and wind stress (**a**) and heat content (SSTA averaged in 0–262 m) (**b**) along the equator in the CFS. When the ATL3 index lagging (leading), the values of the *y*-axis are negative (positive). The contour interval is 0.2

the central and eastern equatorial Atlantic Ocean, that is connected with the STA pattern (Zebiak 1993). The ocean heat content anomaly used in this work is the mean of ocean temperature anomaly from the surface downward to 262 m. The simultaneous correlation pattern of SST and wind stress anomalies with ATL3 index is consistent with that shown in Fig. 7b, and it is similar to the results of Zebiak (1993) (see their Fig. 2). From the lagging and leading correlation, it is shown that the warm water is built up in the western tropical Atlantic in the 9 months prior to the warming peak in the east (Fig. 12a, b). These warm waters over the western tropical Atlantic may be associated with a deepened thermocline forced by Ekman convergence due to the anomalous easterlies (Fig. 12a). In 5–6 months prior to the peak phase of the STA pattern or ATL3 index, as the anomalous equatorial easterlies weaken, positive heat content anomalies develop on the equator. The warm water is transported from the western tropical Atlantic into the equatorial eastern ocean, probably implying an eastward propagating equatorial Kelvin wave signal. The warm water along the central and eastern equator is further developed and reaches its peak in the simultaneous month (Figs. 12a, b) due to a Bjerknes type air–sea interaction (Zebiak 1993).

Meanwhile, cold water is observed in the western ocean in the preceding 2–3 months (Fig. 12b), which may result in the termination of the warm in the central and eastern ocean in the following seasons (Fig. 12b). These results are generally consistent with the corresponding observations (not shown) and previous investigations (Zebiak 1993; Carton and Huang 1994; Huang and Shukla 1997 Handoh and Bigg 2000; Hu and Huang 2007a). Handoh and Bigg (2000) showed that the equatorial fluctuation in the Atlantic from 1995 to 1997 could be explained by coupled air–sea

feedbacks initiated by oceanic wave activities stimulated in the fall of 1995. Moreover, Hu and Huang (2007a) found that there are two centers of SST and wind stress anomalies during the developing phase of the STA pattern. One is along the central equator and the other in the southeastern ocean. The two centers have strong interaction, which account for the fast growth of the pattern.

4.3 Connection with tropics and extratropics

In this subsection, the association of NTA and SSA patterns with the anomalies over the tropics and extratropics in the observations and the CFS is examined and compared. To focus on the NTA pattern and its association with the ENSO and NAO/AO (Arctic Oscillation), we re-calculate the REOF using only MAM mean of the ERv2 analyzed and the CFS simulated SSTA, respectively (Fig. 13). This choice is based on the fact that boreal spring is the season with largest variance of the NTA pattern among the four seasons (Fig. 9). The NTA pattern appears as the first REOF pattern for the ERv2 analyzed SSTA, and second REOF pattern for the CFS simulated SSTA. The first REOF pattern for the CFS simulated SSTA is analogous to a STA-like pattern (not shown). The spatial patterns of the REOF using the MAM mean of the ERv2 analyzed and the

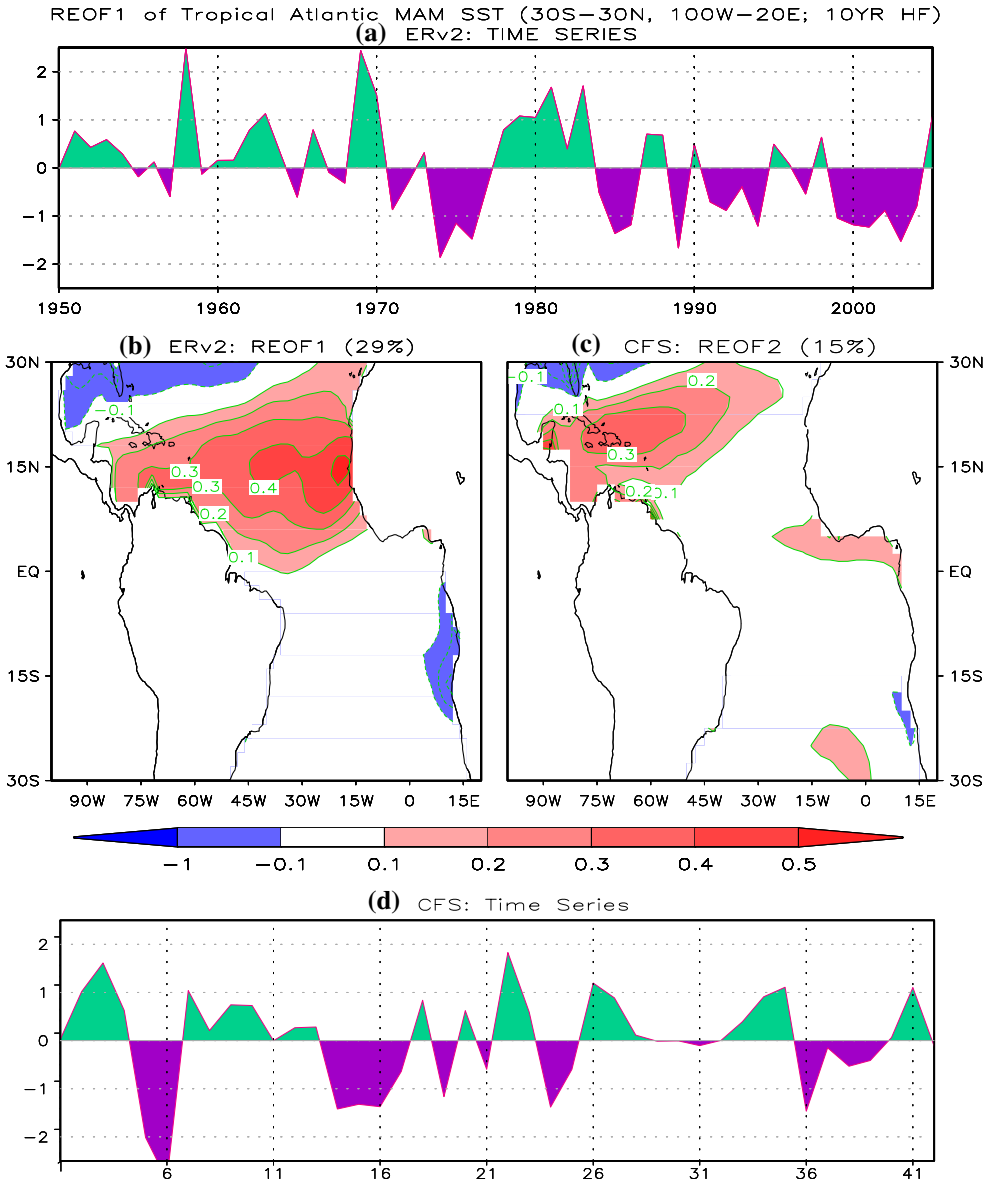

Fig. 13 Spatial patterns and the corresponding time series of REOF1 of ERv2 (**a**, **b**) and REOF2 of the CFS (**c**, **d**) SSTA only in MAM in the tropical Atlantic (30°S–30°N, 100°W–20°E). The contour interval is 0.1°C and the zero line is suppressed. The percentage of the variance explained by this pattern is 29% for the ERv2 SSTA and 15% for the CFS simulated SSTA

CFS simulated SSTA (Fig. 13b, c) are similar to the corresponding ones using all seasonal mean (Figs. 7c, d). To examine the connection of the NTA pattern with tropical and extratropical anomalies, Fig. 14 shows the regressions of sea level pressure (SLP) and wind at 200 hPa (UV200) onto the corresponding time series (Fig. 13a, d). When leading the NTA pattern by 3 and 0 months, the regression patterns for the observations are similar to the corresponding simulation, implying that the CFS captures the major features of the connection of the NTA pattern with tropical and extratropical anomalies (Fig. 14).

Several features in Fig. 14 are worth emphasizing. First, equivalent-barotropic component in the extratropics is dominated in the regressions. Anomalously cyclonic (anti-cyclonic) circulation at 200 hPa corresponds to negative (positive) SLP anomalies. Second, the NTA pattern is linked with NAO/AO-like circulation anomalies. When the NAO/AO are in positive (negative) phase, an anomalously cyclonic (anti-cyclonic) circulation develops in the tropical North Atlantic, favoring positive (negative) SSTA there. This is consistent with Czaja and Frankignoul (2002), Huang and Shukla (2005), Enfield et al. (2006), and Hu and Huang (2006a, 2006b). Third, the NTA pattern is also associated with the anomalies over the western and central Pacific Ocean, implying a link between the ENSO and the NTA pattern. The connection becomes more evident, when

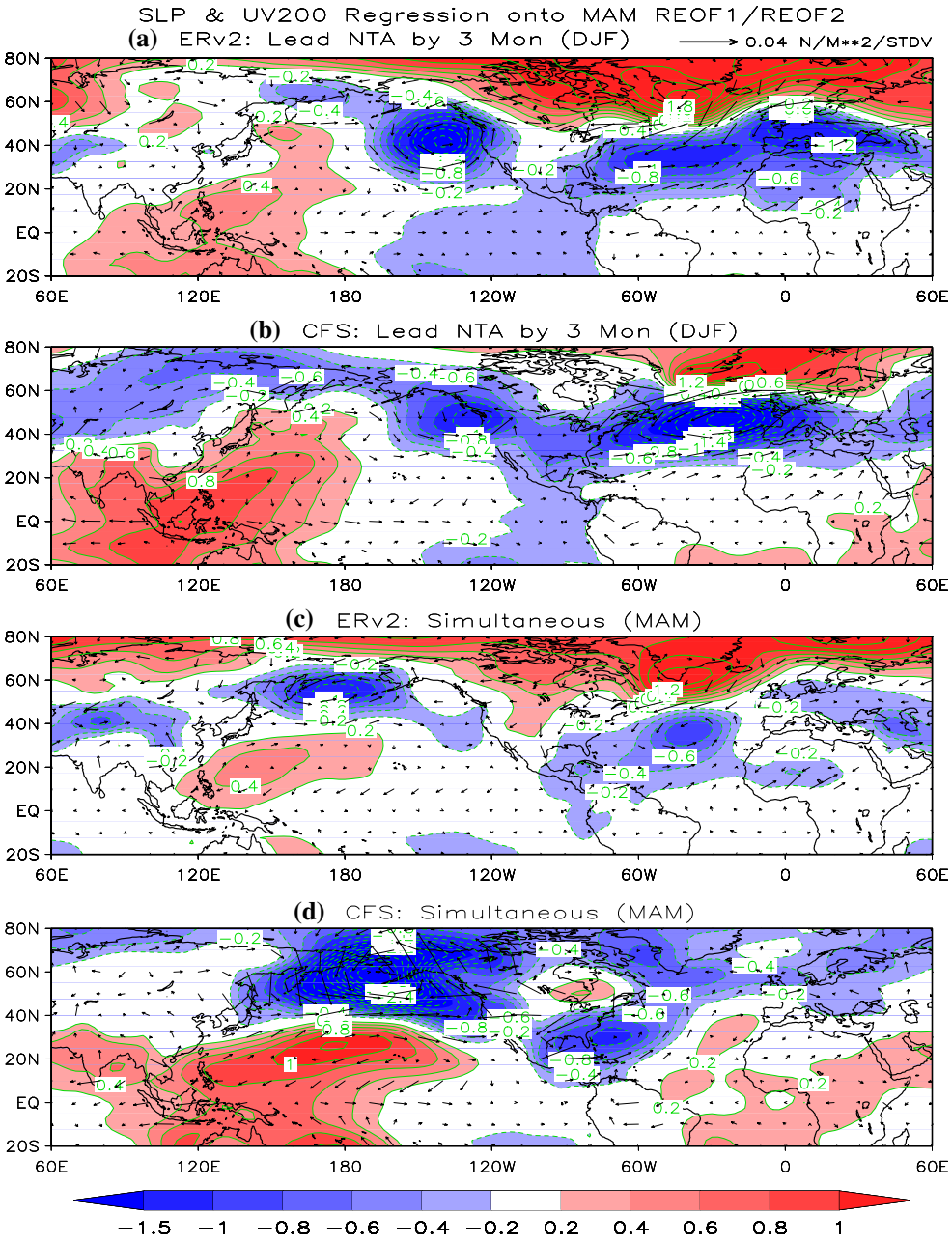

Fig. 14 The regressions of SLP (*contour* and *shading*) and wind at 200 hPa (*vector*) in prior DJF (**a**, **b**) and simultaneous MAM (**c**, **d**) onto the corresponding time series in Fig. 13a and d. The contour interval is 0.2 hPa per STDV and the zero line is suppressed

the regressions are calculated using zonally asymmetric components of SLP and UV200 (Fig. 15). The variability of the NTA pattern is connected with the ENSO via an ENSO induced atmospheric planetary wave train with a PNA-like teleconnection pattern. It is shown that both high latitude anomalies (such as NAO/AO) and ENSO can affect the climate variability in the tropical North Atlantic Ocean. This is in line with previous investigations, such as, Enfield and Mayer (1997), Saravanan and Chang (2000), Huang et al. (2002), Czaja et al. (2002), Xie and Carton (2004).

There are some differences in the simulated oceanic and atmospheric patterns associated with the NTA relative to the observations. In particular, on average, the connection of the NTA pattern in MAM with SLP and UV200 in preceding DJF (Figs. 14a, b, 15a, b) is stronger than that with SLP and UV200 in the simultaneous MAM (Figs. 14c, d, 15c, d). This is consistent with the forcing-response relationship between the atmosphere and the Atlantic Ocean. The seasonal dependence may be due to the seasonal migration of mean flow that affects the wave propagation and also due to the larger climate variability in

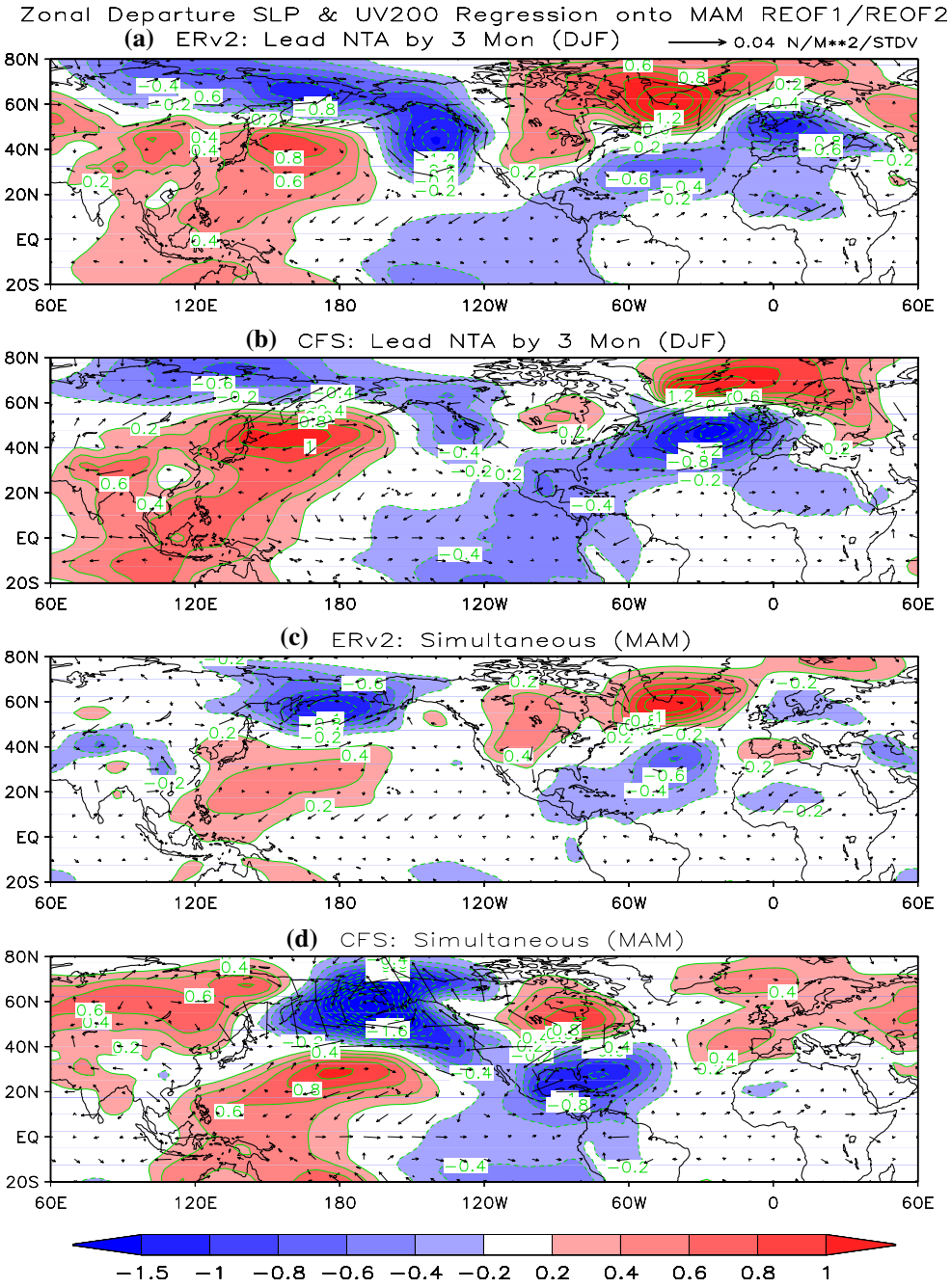

Fig. 15 Same as Fig. 14, but for zonally asymmetric components of SLP and wind at 200 hPa

DJF than in MAM in the NH. The negative center in the tropical North Atlantic Ocean is shifted southwestward from preceding DJF to MAM in both the observations and simulation. In addition to the intensity difference of these regressions, there are some detailed differences in the locations of the individual centers between the observations and the simulation in Figs. 14 and 15, which may be related to differences in the specific location of the wave sources and the structure of mean circulation.

Similarly, we analyzed the SSA pattern in DJF and its connection with the tropical and extratropical anomalies in the SH (Figs. 16, 17, 18). We focus on DJF due to the fact that the SSA pattern has the largest variability during that season (Fig. 9). The spatial pattern for DJF only (Figs. 16b, c) is analogous to that of the all season mean (Fig. 7e, f). The major difference of the spatial pattern between the CFS simulation and the observations is the northwestward displacement of the center in both the DJF and all season means of the CFS. The SLP and UV200 anomalies associated with the SSA pattern displays a zonally symmetric structure, which is similar to the Antarctic Oscillation (AAO) (Gong and Wang 1999) or southern annular mode (SAM) (Thompson et al. 2000; Thompson and Wallace 2000; Visbeck and Hall 2004). Gong and Wang (1999) defined an Antarctic Oscillation Index using the difference of zonal mean SLP between 40°S and 65°S to measure the large scale alternation of atmospheric mass between the mid-latitudes and high latitudes. Hall and Visbeck (2002)

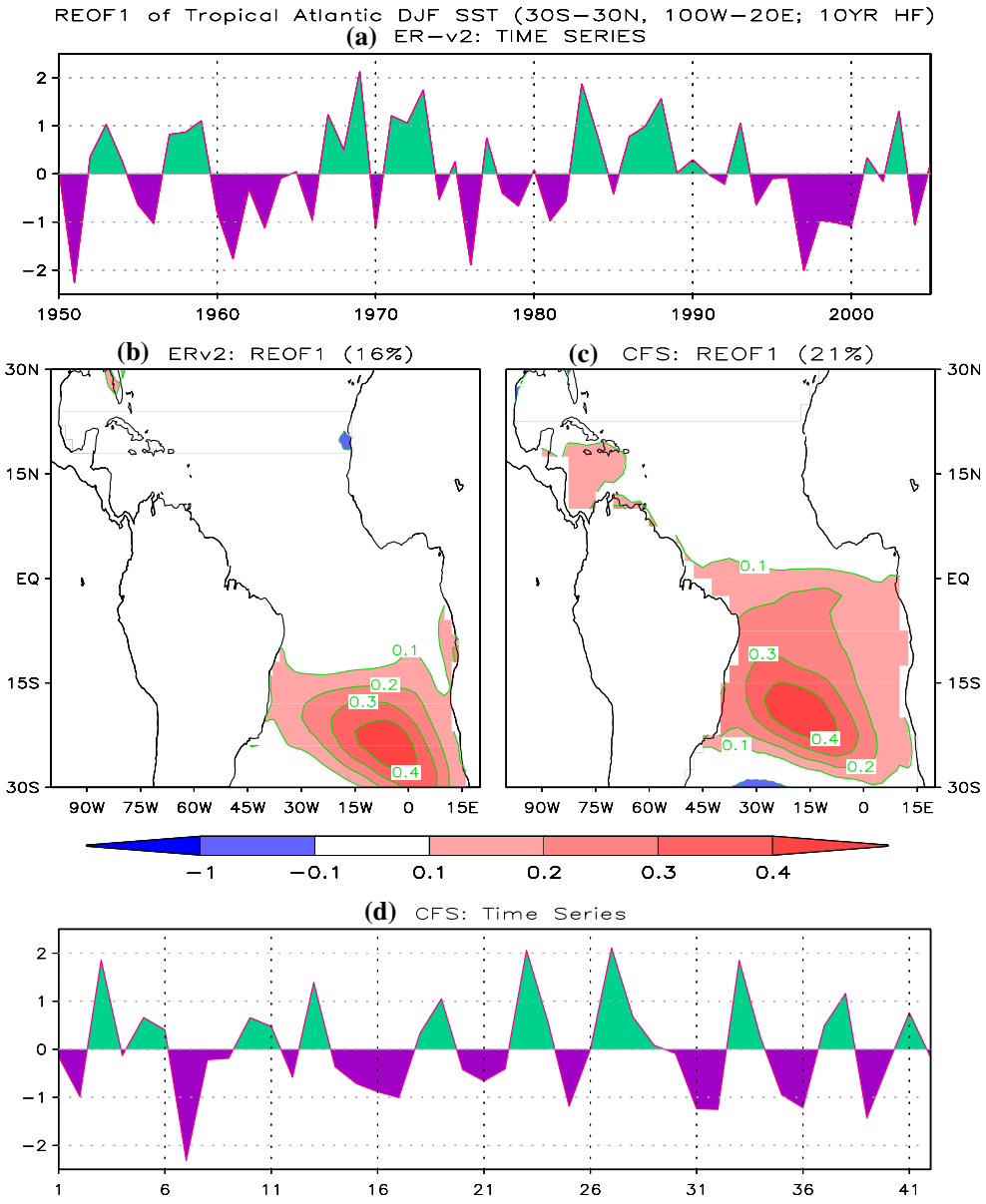

Fig. 16 Spatial patterns and the corresponding time series of REOF1 of ERv2 (**a**, **b**) and the CFS (**c**, **d**) SSTA only in DJF in the tropical Atlantic (30°S–30°N, 100°W–20°E). The contour interval is 0.1°C and the zero line is suppressed. The percentage of the variance explained by this pattern is 16% for the ERv2 SSTA and 21% for the CFS simulated SSTA

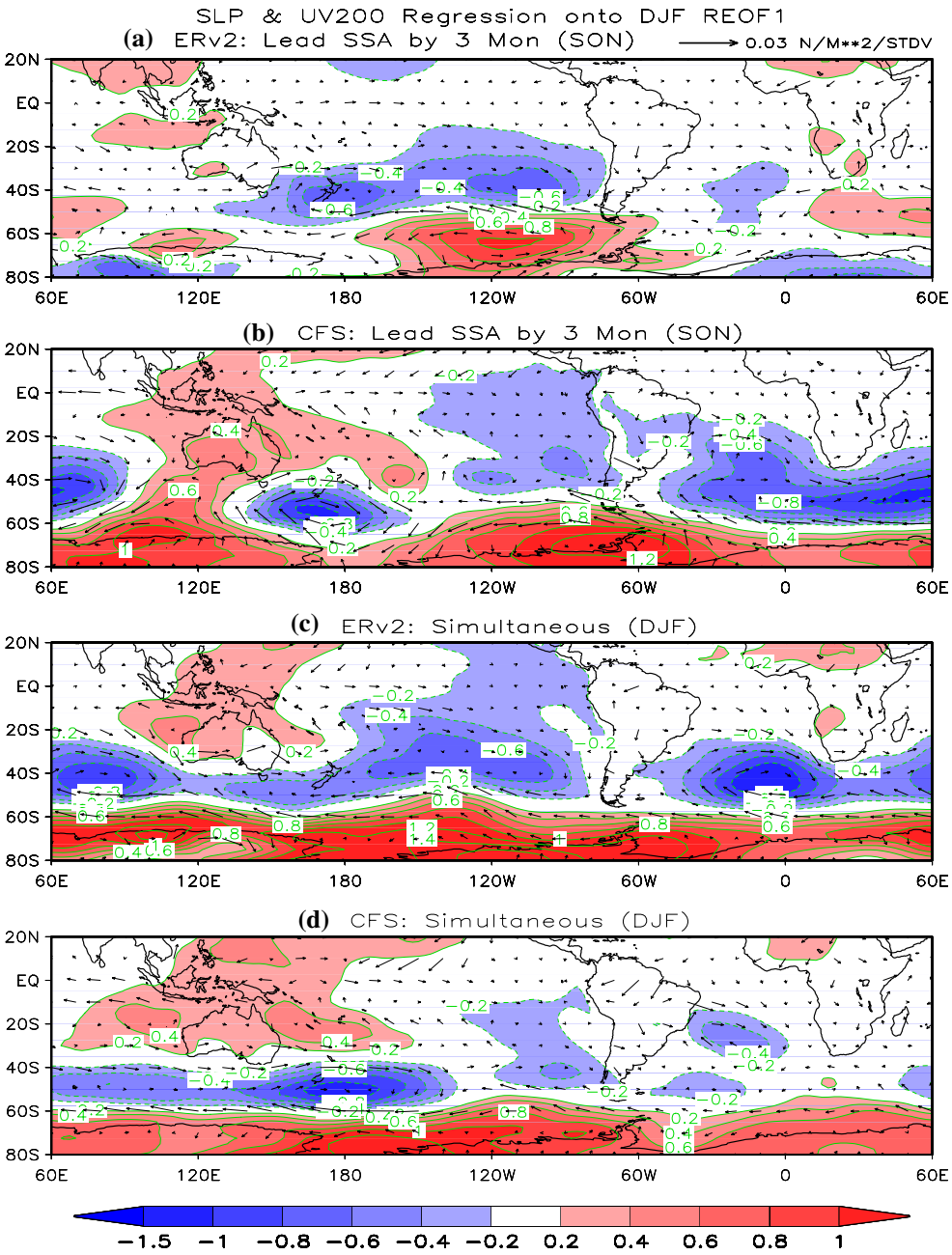

Fig. 17 The regressions of SLP (*contour* and *shading*) and wind at 200 hPa (*vector*) in prior SON (**a**, **b**) and simultaneous DJF (**c**, **d**) onto the corresponding time series in Figs. 16a and d. The contour interval is 0.2 hPa per STDV and the zero line is suppressed

documented that the SAM can generate ocean circulation and sea ice variations in a coarse-resolution CGCM. It is interesting to note that the symmetric component is larger in the simultaneous (DJF) regressions (Fig. 17c, d) than in the regression in the preceding SON (Figs. 17a, b) in both the CFS simulation and the observations.

The corresponding regressions of zonally asymmetric components (Fig. 18) suggest a connection of the SSA pattern with low-latitude anomalies. In the preceding SON (Fig. 18a, b), the major positive anomalies exist in southwestern Australia and in the subpolar regions of the South Pacific Ocean. Negative anomalies exist around New Zealand and in the subpolar regions of the South Atlantic Ocean. In the simultaneous regressions (Fig. 18c, d), the anomalies are weakened, except for the negative anomalies in the South Atlantic Ocean. These negative anomalies are intensified and shifted equatorward from the preceding SON to DJF. The positive SSTA is developed on the equatorial side of the negative anomaly center of SLP and connected with anomalously cyclonic circulation at 200 hPa. The contrast of the location of the negative anomalous center of SLP and the associated anomalous cyclonic circulation at 200 hPa between the CFS simulation and the observations (Fig. 18c, d) is consistent with the spatial pattern of the SSA shown in Figs. 7e and f.

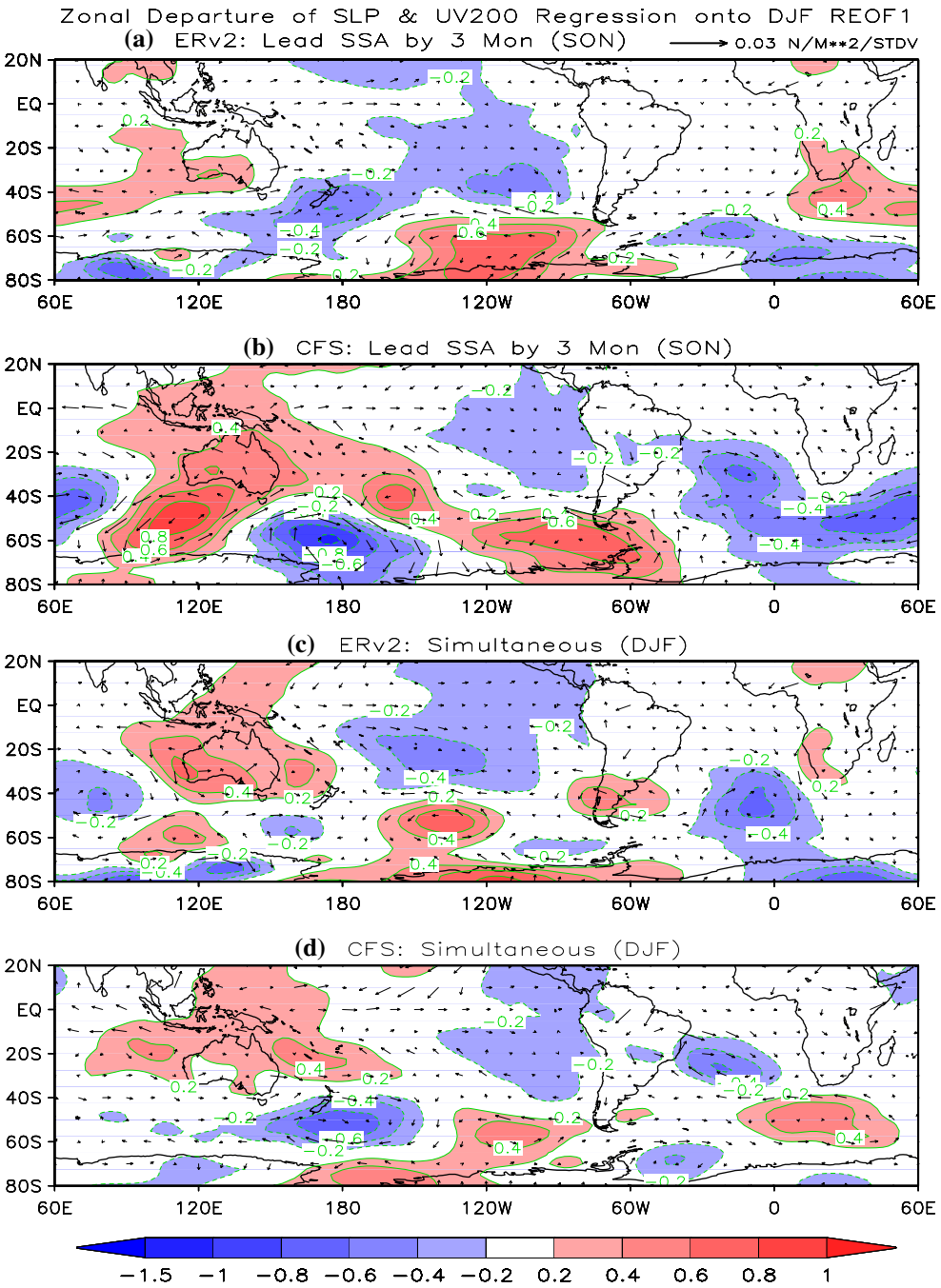

Fig. 18 Same as Fig. 17, but for zonally asymmetric parts of SLP and wind at 200 hPa

Current results of the teleconnection associated with the South Atlantic variability (SSA pattern) are consistent with the series of previous investigations of Mo and White (1985), Mo and Higgins (1998), Mo (2000), and Mo and Häkkinen (2001). Mo and White (1985) argued that the anomalies over Australia are connected with the anomalies over the South American continent (see their Fig. 8). Mo and Hoggins (1998) identified two eastward propagating Pacific-South American (PSA) patterns in the SH winter and Mo (2000) further linked them to tropical convection as well as the SSTA. Mo and Häkkinen (2001) indicated that the interannual variability in both the tropical North and South Atlantic is influenced by the anomalies in the tropical Pacific Ocean through different time scale processes. They found that the SSTA in the tropical North Atlantic are associated with the quasi-biennial component of ENSO with a time scale of 22–23 months. In the tropical South Atlantic, it is influenced by the low-frequency part of the ENSO signal with a time scale of 36–48 months.

The above analyses suggest that the primary feature of the distribution pattern of SLP and UV200 in the NH associated with the NTA pattern (Figs. 14, 15) resembles that in the SH (Figs. 17, 18) linked with the SSA pattern. It implies that there is a similarity of the mechanisms in the evolution of the NTA and SSA patterns and their connection with the tropical and high latitude anomalies in their respective hemisphere. The anomalies associated with both the SSA and NTA patterns are dominated by equivalent-barotropic disturbances in the extratropics and connected with zonally symmetric and asymmetric variability. The zonally symmetric variation is associated with the AO in the NH and the AAO in the SH. The zonally asymmetric part of the anomalies in the Atlantic is teleconnected with the anomalies over the tropical Pacific.

5 Summary and discussion

Correctly simulating the mean annual cycle and the leading patterns of the tropical Atlantic Ocean variability is still a challenge for current state-of-the-art CGCMs. This paper examines the mean annual cycle, interannual variability, and leading patterns of the tropical Atlantic Ocean simulated in a long-term integration of the CFS. This model is a state-of-the-art CGCM presently used for operational climate prediction at NCEP. By comparing the CFS simulation with corresponding observation-based analyses or reanalyses, it is shown that the CFS captures the seasonal mean climate. Specifically the CFS reproduces the zonal gradients of SST along the equatorial Atlantic Ocean, even though that the CFS produces warm biases and underestimates the variability over the southeastern ocean. The seasonal transition from warm to cold phase along the equator is delayed 1 month in the CFS compared with the observations. This might be related to the model failure in simulating the cross-equator meridional wind associated with the African monsoon.

The CFS also realistically simulates both the spatial structure and spectral distributions of the three major leading patterns of SSTA in the tropical Atlantic Ocean. The CFS simulates the seasonal dependence of these patterns and partially reproduces their association with ENSO. The dynamical and thermodynamical processes associated with these patterns in the simulation and the observations are similar. The air–sea interaction processes associated with the STA pattern are well simulated in the CFS. The primary feature of the anomalous circulation in the NH associated with the NTA pattern resembles that in the SH linked with the SSA pattern. This implies that the mechanisms in the evolution of the NTA and SSA patterns and their connection with the tropical and extratropical anomalies in their respective hemispheres are similar. The anomalies associated with both the SSA and NTA patterns are dominated by atmospheric fluctuations of equivalent-barotropic structure in the extratropics including zonally symmetric and asymmetric components. The zonally symmetric variability is associated with the annular modes, AO in the NH and AAO in the SH. The zonally asymmetric part of the anomalies in the Atlantic is teleconnected with the anomalies over the tropical Pacific. The misplaced teleconnection center over the southern subtropical ocean may be one of the reasons for the deformation of the SSA pattern in the CFS.

Although significant progress in simulating the tropical mean climatology and its variability has been achieved in the past decade, tropical biases are still large and remain an unresolved problem for current state-of-the-art CGCMs. Some attempts have been made to further analyze or eliminate the biases. For example, Hazeleger and Haarsma (2005) found that the simulation of tropical Atlantic variability as expressed in the meridional gradient mode and the eastern cold tongue mode improves when the entrainment efficiency in their coupled model is enhanced. Jochum and Murtugudde (2006) used a numerical model of the tropical Pacific Ocean and investigated the processes that cause the horizontal temperature advection of tropical instability waves (TIW). It is found that the TIW can affect the heat budget of the oceanic mixed layer. Thus, the TIW may be a factor associated with the tropical SST bias generation. Recently, Huang et al. (2007) demonstrated that the biases of the CFS hindcasts in the southeastern Atlantic Ocean reach their peak in boreal winter. These biases are mainly caused by the fact that the CFS produces too little low-cloud cover in the southeastern tropical Atlantic Ocean from boreal summer to winter, leading to an overestimate of the amount of local solar radiation reaching the sea surface and resulting in the warm SST bias. The underestimation of low clouds in the CFS is related to an incorrected vertical temperature stratification in the lower troposphere (Hu et al. 2007c). Xie et al. (2007) argued that the interaction of low cloud and SST is an important internal feedback for the climate asymmetry between the NH and SH. In one of their experiments, they found that turning off the cloud radiation effects in their model weakens the climate asymmetry and reduces north–south migration of the ITCZ. We plan to do some experiments to investigate the influence of low clouds on the evolution of the biases in the tropical Atlantic.

Acknowledgments The authors appreciate the comments and suggestions of B. Klinger and D. Straus which significantly improved the manuscript. This work was supported by the NOAA CLIVAR Program (NA04OAR4310115 and NA07OAR431031) and the GEC-hri project (NASA Grant NNX06AF30G, Mason project 201152-1).

References

Breugem WP, Hazeleger W, Haarsma RJ (2006) Multimodel study of tropical Atlantic variability and change. Geophys Res Lett 33:L23706. DOI 10.1029/2006GL027831

Carton JA, Huang B (1994) Warm events in the tropical Atlantic. J Phys Oceanogr 24:888–903

Chang P, Ji L, Li H (1997) A decadal climate variation in the tropical Atlantic Ocean from thermodynamic air–sea interactions. Nature 385: 516–518

Chang P, Fang Y, Saravanan R, Ji L, Seidel H (2006) The cause of the fragile relationship between the Pacific El Niño and the Atlantic Niño. Nature 443:324–328. DOI 10.1038/nature05053

Czaja A, Frankignoul C (2002) Observed impact of Atlantic SST anomalies on the North Atlantic Oscillation. J Clim 15:606–623

Czaja A, van der Vaart P, Marshall J (2002) A diagnostic study of the role of remote forcing in tropical Atlantic variability. J Clim 15: 3280–3290

Davey MK et al. (2002) STOIC: a study of coupled model climatology and variability in tropical ocean regions. Clim Dyn 18:403–420. DOI 10.1007/s00382-001-0188-6

Delworth TL, et al. (2006) GFDL's CM2 global coupled climate models—part I: formulation and simulation characteristics. J Clim 19:643–674

Deser C, Capotondi A, Sravanan R, Phillips AS (2006) Tropical Pacific and Atlantic climate variability in CCSM3. J Clim 19:2451–2481

Enfield DB, Mayer DA (1997) Tropical Atlantic sea surface temperature variability and its relation to the El Niño-Southern Oscillation. J Geophys Res 102(C1):929–945

Enfield DB, Lee S-K, Wang C (2006) How are large Western Hemisphere warm pools formed? Progr Oceanogr 70(2–4):346–365

Gnanadesikan A, et al. (2006) GFDL's CM2 global coupled climate models—part II: the baseline ocean. J Clim 19:675–697

Gong DY, Wang SW (1999) Definition of Antarctic oscillation index. Geophys Res Lett 26:459–462

Hall A, Visbeck M (2002) Synchronous variability in the Southern Hemisphere atmosphere, sea ice, and ocean resulting from the annular mode. J Clim 15:3043–3057

Handoh IC, Bigg GR (2000) A self-sustaining climate mode in the tropical Atlantic, 1995–1997: observations and modelling. Q J R Meteorol Soc 126 (564):807–821

Hazeleger W, Haarsma RJ (2005) Sensitivity of tropical Atlantic climate to mixing in a coupled ocean–atmosphere model. Clim Dyn 25 (4):387–399. DOI 10.1007/s00382-005-0047-y

Hong S-Y, Pan H-L (1998) Convective trigger function for a mass-flux cumulus parameterization scheme. Mon Weather Rev 126:2599–2620

Hu Z-Z, Huang B (2006a) Air–sea coupling in the North Atlantic during summer. Clim Dyn 26(2):441–457. DOI 10.1007/s00382-005-0094-4

Hu Z-Z, Huang B (2006b) Physical processes associated with tropical Atlantic SST meridional gradient. J Clim 19 (21):5500–5518

Hu Z-Z, Huang B (2007a) Physical processes associated with tropical Atlantic SST gradient during the anomalous evolution in the southeastern ocean. J Clim 20 (14):3366–3378

Hu Z-Z, Huang B (2007b) The predictive skill and the most predictable pattern in the tropical Atlantic: The effect of ENSO. Mon Weather Rev 135 (5):1786–1806

Hu Z-Z, Huang B, Pegion K (2007c) Low cloud errors over the southeastern Atlantic in the NCEP CFS and their association with lower-tropospheric stability and air-sea interaction. J Geophys Res (Ocean) (in press)

Huang B, Shukla J (1997) Characteristics of the interannual and decadal variability in a general circulation model of the tropical Atlantic Ocean. J Phys Oceanogr 27:1693–1712

Huang B, Shukla J (2005) Ocean–atmosphere interactions in the tropical and subtropical Atlantic Ocean. J Clim 18:1652–1672

Huang B, Schopf PS, Pan Z (2002) The ENSO effect on the tropical Atlantic variability: a regionally coupled model study. Geophys Res Lett 29(21):2039. DOI 10.1029/2002GL014872

Huang B, Schopf PS, Shukla J (2004) Intrinsic ocean–atmosphere variability of the tropical Atlantic Ocean. J Clim 17:2058–2077

Huang B, Hu Z-Z, Jha B (2007) Evolution of model systematic errors in the tropical Atlantic basin from the NCEP coupled hindcasts. Clim Dyn 28 (7/8):661–682. DOI 10.1007/s00382-006-0223-8

Illig S, Gushchina D, Dewitte B, Ayoub A, du Penhoat Y (2006) The 1996 equatorial Atlantic warm event: Origin and mechanisms. Geophys Res Lett 33:L09701. DOI 10.1029/2006GL025632

Jochum M, Murtugudde R (2006) Temperature advection by tropical instability waves. J Phys Oceanogr 36:592–605

Jungclaus JH, Keenlyside N, Botzet M, Haak H, Luo J-J, Latif M, Marotzke J, Mikolajewicz U, Roeckner E (2006) Ocean circulation and tropical variability in the coupled model ECHAM5/MPI-OM. J Clim 19:3952–3972

Kalnay E, Kanamitsu M, Kistler R, Collins W, Deaven D, Gandin L, Iredell M, Saha S, White G, Woollen J, Zhu Y, Chelliah M, Ebisuzaki W, Higgins W, Janowiak J, Mo KC, Ropelewski C, Wang J, Leetmaa A, Reynolds R, Jenne R, Joseph D (1996) The NCEP/NCAR 40-year reanalysis project. Bull Am Meteorol Soc 77:437–471

Mitchell TP, Wallace JM (1992) On the annual cycle in equatorial convection and sea surface temperature. J Clim 5:1140–1156

Mo KC (2000) Relationships between low-frequency variability in the Southern Hemisphere and sea surface temperature. J Clim 13:3599–3610

Mo KC, Häkkinen S (2001) Interannual variability in the tropical Atlantic and linkages to the Pacific. J Clim 14(12):2740–2762

Mo KC, Higgins RW (1998) The Pacific-South American modes and tropical convection during the Southern Hemisphere winter. Mon Weather Rev 126: 1581–1596

Mo KC, White GH (1985) Teleconnections in the Southern Hemisphere. Mon Weather Rev 113:22–37

North GR, Bell TL, Cahalan RF, Moeng FJ (1982) Sampling errors in the estimation of empirical orthogonal functions. Mon Weather Rev 110: 699–706

Okumura Y, Xie S-P (2004) Interaction of the Atlantic equatorial cold tongue and the African monsoon. J Clim 17:3589–3602

Pacanowski RC, Griffies SM (1998) MOM 3.0 manual, NOAA/Geophysical Fluid Dynamics Laboratory, Princeton, New Jersey, USA 08542, 668 pp

Press WT, Teukolsky SA, Vetterling WT, Flannery BP (1992) Numerical Recipes in fortran, the art of scientific computing, 2nd Edn. Cambridge University Press, Cambridge, pp 1–963

Richman MB (1986) Rotation of principal component. J Climatol 6: 293–335

Ruiz-Barradas A, Carton JA, Nigam S (2000) Structure of interannual-to-decadal climate variability in the Tropical Atlantic sector. J Clim 13:3285–3297

Saha S, Nadiga S, Thiaw C, Wang J, Wang W, Zhang Q, van den Dool H, Pan H-L, Moorthi S, Behringer D, Stokes D, Pena M, Lord S, White G, Ebisuzaki W, Peng P, Xie P (2006) The NCEP climate forecast system. J Clim 19(5):3483–3517

Saravanan R, Chang P (2000) Interaction between tropical Atlantic variability and El Niño-Southern Oscillation. J Clim 13:2177–2194

da Silva A, Young CC, Levitus S (1994) Atlas of Surface Marine Data 1994. Vol. 1: Algorithms and Procedures. NOAA Atlas NESDIS 6, U. S. Department of Commerce, Washington, DC, 83 pp

Smith TM, Reynolds RW (2003) Extended reconstruction of global sea surface temperatures based on COADS data (1854–1997). J Clim 16: 1495–1510

Sterl A, Hazeleger W (2003) Coupled variability and air–sea interaction in the South Atlantic. Clim Dyn 21:559–571

Thompson DWJ, Wallace JM (2000) Annular modes in the extratropical circulation. Part I: Month-to-month variability. J Clim 13:1000–1016

Thompson DWJ, Wallace JM, Hegerl G (2000) Annular modes in the extratropical circulation. Part II: Trends. J Clim 13:1018–1036

Venegas SA, Mysak LA, Straub DN (1997) Atmosphere–ocean coupled variability in the South Atlantic. J Clim 10:2904–2920

Visbeck M, Hall A (2004) Reply. J Clim 17:2255–2258

Wang W, Saha S, Pan H-L, Nadiga S, White G (2005) Simulation of ENSO in the new NCEP coupled forecast system model. Mon Weather Rev 133: 1574–1593

Woodruff SD, Slutz RJ, Jenne RL, Steurer PM (1987) A comprehensive ocean–atmosphere data set. Bull Am Meteor Soc 68:1239–1250

Wu L, Zhang Q, Liu Z (2004) Toward understanding tropical Atlantic variability using coupled modeling surgery. In: Wang C, Xie S-P, Carton JA (eds) Earth's climate: The ocean–atmosphere interaction. Geophysical monograph, no. 147, Am Geophys. Union, Washington DC, pp 157–170

Xie S-P (1999) A dynamic ocean–atmosphere model of the tropical Atlantic decadal variability. J Clim 12:64–70

Xie P, Arkin PA (1996) Analyses of global monthly precipitation using gauge observations, satellite estimates, and numerical model predictions. J Clim 9:840–858

Xie S-P, Carton JA (2004) Tropical Atlantic variability: Patterns, mechanisms, and impacts. In: Wang C, Xie S-P, Carton JA (eds) Earth's Climate: The Ocean–Atmosphere Interaction. Geophysical Monograph, No. 147, Amer Geophys. Union, Washington DC, pp 121–142

Xie S-P, Philander SGH (1994) A coupled ocean–atmosphere model of relevance to the ITCZ in the eastern Pacific. Tellus 46A:340–350

Xie S-P, Miyama T, Wang Y, Xu H, de Szoeke SP, Small RJO, Richards KJ, Mochizuki T, Awaji T (2007) A regional ocean-atmosphere model for eastern Pacific climate: toward reducing tropical biases. J Clim 20: 1504–1522

Zebiak SE (1993) Air–sea interaction in the equatorial Atlantic region. J Clim 6:1567–1586